Physics Department

Research Work

Characterization Techniques for Scientific Charge-Couple Devices

Julia Campa Romero

Director: Francisco Javier Castander (ICE-CSIC/IEEC)

Tutor: Enrique Fernandez (IFAE)

October 2007

Universitat Autonoma de Barcelona

Contents

1 Prologue

Charge Couples Devices, or CCDs, have many applications but a remarkable one is their use in modern day astronomy. In the telescopes they produce amazing astronomical images. The aim of this work is to describe the system to characterize these devices as well as some techniques to test them before being installed in the focal plane of the Blanco telescope in Cerro Tololo (Chile). These tasks are done in the CCD testing facility at Fermi National Accelerator Laboratory (Fermilab).

I was involved in Barcelona and Fermilab in the initial phase that it is important to learn and develop the infrastructure and experience for the production phase, when the devices will be characterized to determine the best ones that should populate the focal plane. During the first phase in Barcelona, a CCD-testing dewar identical to the Fermilab's one was built to test the new electronics boards of the data acquisition system that will be used in the instrument with CCDs. The work that will be described in this document includes the mechanical construction and the vacuum and cryogenic system control that it used to cool down the devices.

This work also describes how the engineering grade CCDs for DECam are compared with the technical specifications for the Dark Energy Survey and how the camera is calibrated. Detailed performance measurements for comparison with the specifications are presented for a few example CCDs. I will only describe the techniques and methods in which I was involved and in which I took data. These are part of first stage tests before the CCDs are installed in the focal plane. If the devices pass these first stage tests more detailed studies will be done.

2 Introduction and Overview

2.1 The DES Project

2.1.1 Theoretical Background. The Science Context of the Dark Energy Survey.

A critical research problem in cosmology is the need to understand the accelerating expansion of the Universe. This acceleration requires something new called Dark Energy, which could arise from the energy of the vacuum (the cosmological constant) or a new ultra-light particle; alternatively it could indicate a flaw in Einstein's General Relativity, perhaps signaling that our three-dimensional world is embedded in a Universe of higher spatial dimensions. Any of these possibilities would represent a boost in our current understanding of the nature of matter, energy, space, and time. In order to sort out the possibilities and pin down the nature of the Dark Energy, we need to make more precise measurements of its properties. The key property of dark energy that determines the expansion history of the Universe is its equation of state parameter, w, the ratio of its effective pressure to its energy density. In order to precisely measure w and its possible time evolution, a powerful new instrument is going to be built and a flexible and responsive data management system to accompany it.

The goal of the Dark Energy Survey (DES) is to perform a 5000 sq. deg. g, r, i, z imaging survey of the Southern Galactic Cap in order to constrain the Dark Energy equation-of-state parameter $w = P/\rho$ to less than 5 % (statistical errors) in each of four

complementary techniques and to begin to constrain the derivative of w with respect to the redshift (dw/dz). The four methods are: galaxy clusters, weak gravitational lensing tomography, galaxy angular clustering, and supernova distances. By deriving the four sets of measurements from the same data set with a common analysis framework, it will be obtained important cross-checks of the systematic errors and thereby make a substantial and robust advance in the precision of dark energy measurements.

2.1.2 The DES instrument (DECam)

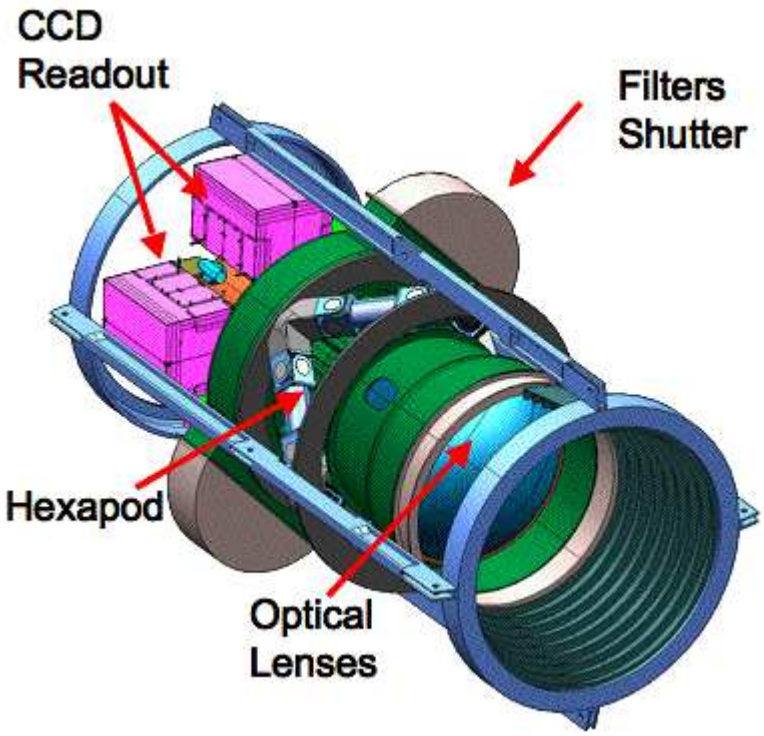

Figure 1: DES Instrument

The survey will use the Blanco 4m telescope at Cerro Tololo Interamerican Observatory (CTIO) in order to achieve the goal of surveying $1/4$of the Southern sky.

The major components of DECam are a 520 megapixel optical CCD camera with vacuum and cryogenic controls, a compact low noise CCD readout system housed in actively cooled crates, a combination shutter-filter system to house the shutter, the four DES filters (g, r, i, z) and slots for four additional filters that could be provided by the observer community, and a wide-field optical corrector (2.2^0 field of view). The imager and corrector barrels are supported as a single unit by a 6×6 hexapod that will provide lateral adjustability as well as focus control.

The DES survey strategy is based on taking multiple short exposures (100 - 400 s) and adding them together to reach the required depth in each filter pass-band. This strategy minimizes the systematic uncertainties resulting from effects such as atmospheric variations. In the first two years it is planned to tile the entire survey area multiple times to enable early scientific results. To maximize the total time available for exposures, we plan to read out the image CCDs while the telescope is slewing to a new position. Current measurements indicate that the time it takes for a typical DES slew of 2^o is $\sim$ 35 s. Upgrades planned by CTIO for the telescope control system will likely reduce this to 17 s. At the projected CCD readout rate of 250 kpix/sec, the total readout will take 17 s and will match the improved telescope slew time. The alignment and focus CCDs are planned to be read out with the image CCDs to allow for image by image corrections. Currently at the Blanco, observations are interrupted 2, 3 times per night to correct the telescope focus; the corrector-primary mirror alignment is checked and adjusted every few months. Experience with DECam on the Blanco will determine the frequency at which corrections are needed to maintain the best image quality. The guide CCDs need to provide signals to the telescope control systems at a rate of $\sim$ 1 Hz. To achieve this rate, exposures of $\sim$ 0.5 s are envisioned and only a small area centered on the guide star will be read out.

The focal plane consists of 62 2048$\times$4096 pixel CCD modules (0.27 ”/pixel) arranged in a hexagonal sensitive area. The schematic of the plane is shown in Fig. 2 compared with an image of the moon taken with the existing MOSAIC 8 CCD camera at Blanco (CTIO). The DES focal plane, also has smaller format CCDs for guiding (G), focusing (F) and alignment (WF) that are located at the edges of the focal plane.

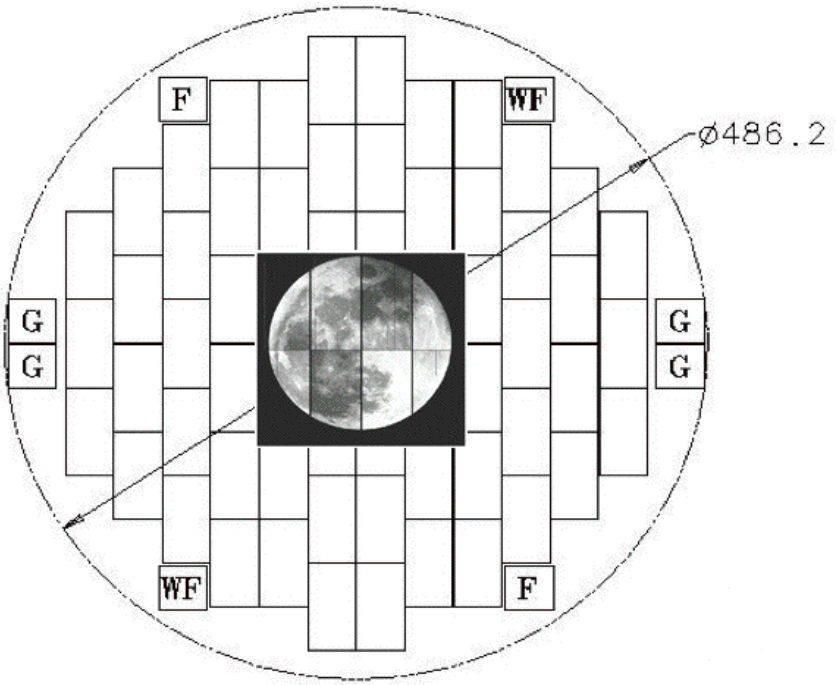

Figure 2: DES Focal Plane

2.1.3 The DES CCDs. Characteristics, Background, Fabrication and Packaging.

The CCDs have a front-side, where all the gate structures and buried channel layers are deposited, and a back-side, which is simply bulk silicon generally covered with a thin conductive layer. The devices thickness, of the order of 100-300 μm, make these chips relatively high in their susceptibility to detection of cosmic rays. Because the photons must first pass through the gate structures before they can be absorbed by the silicon, front-side-illuminated CCDs have lower overall quantum efficiencies than the back-side-illuminated devices.

In the latter CCDs the incoming photons can be absorbed directly into the bulk silicon pixels without the interference of the gate structures. The advantages in this type of CCD are that their relative quantum efficiency greatly exceeds the one of a front-side device and the response of the detector to shorter wavelength light is improved since the photons no longer need to pass through the pixel gates.

The quantum efficiency is the ratio of incident photons to generate electron-holes pairs. To obtain z-band (700 nm to 1000 nm) images efficiently for high-redshift (z$\sim$ 1.3) galaxies, the fully depleted, high-resistivity, 250 μm thick, 15 μm pixel size and back illuminated CCDs that have been designed and developed at the Lawrence Berkeley National Laboratory (LBNL) have been selected. The thickness of the LBNL design has two important implications for DES: fringing is eliminated, and the quantum efficiency (QE) of these devices is > 50% in the z band, a factor of 5-10 higher

than traditional thinned astronomical devices as is shown in Fig. 3.

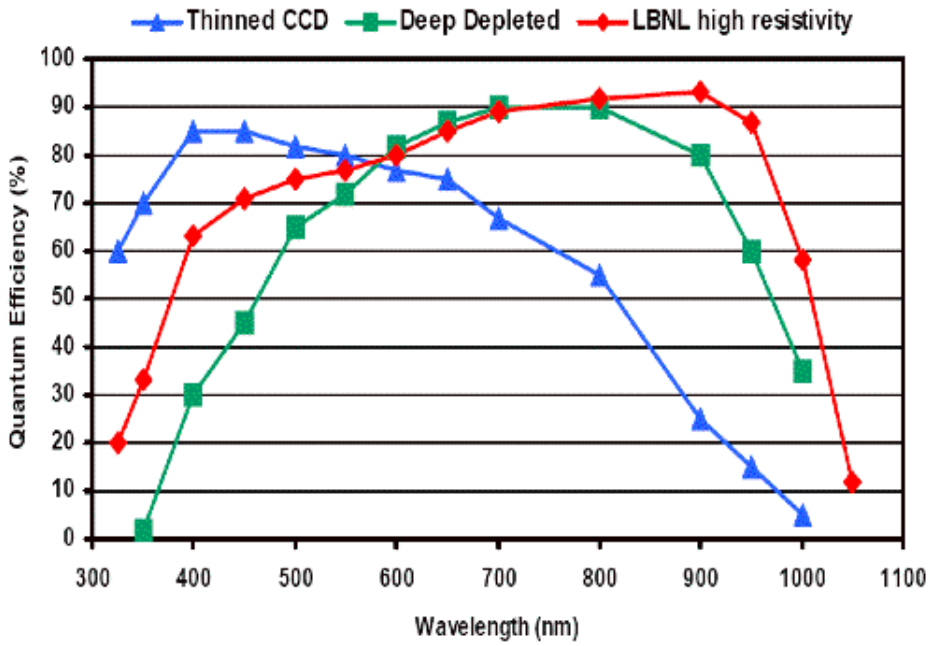

Figure 3: Quantum efficiency of Thinned, Deep Depleted and LBNL high resistivity CCDs.

The absorption length is the distance into the CCD where 63% $(1 - e^{-1})$ of the photons are absorbed at a specified wavelength, therefore the quantum efficiency is related with this parameter or with the thickness of the CCD. The Fig. 4 shows the calculated absorption length in silicon as a function of wavelength and how it increases with that. At some photon energies the absorption length can be more than 100 μm requiring thick CCDs to achieve high quantum efficiency in the near-infrared.

In thinned CCDs fringing arises due to multiple reflections at long wavelengths when the absorption of the incident light is greater than the CCD thickness. In a thinned CCD, the absorption length of light exceeds the thickness of the active region at $\lambda \gtrsim$ 870 nm, resulting in both fringing and decreasing QE for longer wavelengths. For this 250 μm CCDs this occurs at more than 1000 μm. A good blue response is reached by choosing a back illuminated design so that no gate structure absorbs the UV light. Fig. 5 shows a schematic cross section of the LBNL CCD compared with other conventional designs. In this work the type of CCD that will be tested is the p-channel thick back illuminated CCD although for the initial phase thicker p-channel CCDs of 650 μm have also been tested with front illumination. The latter are the same as the former but without the processing to make them thinner and back illuminated.

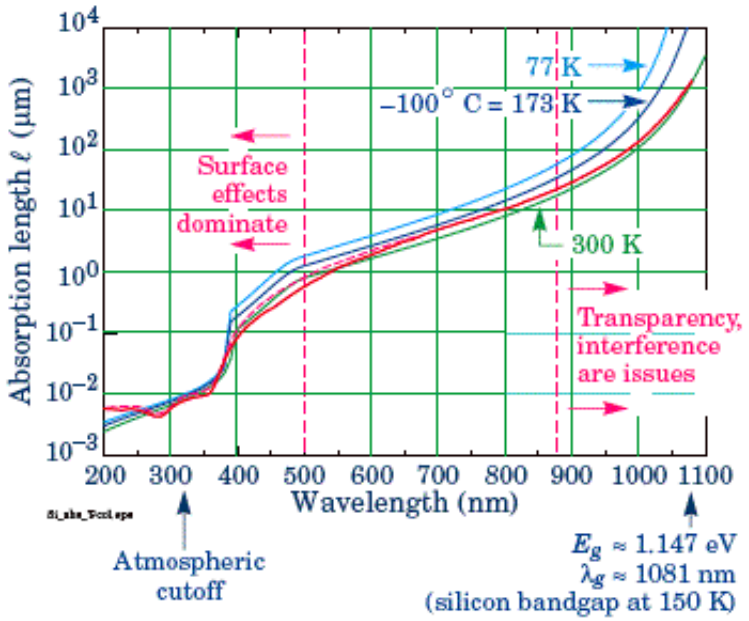

Figure 4: Absorption length versus wavelength for silicon. (LBLN graph)

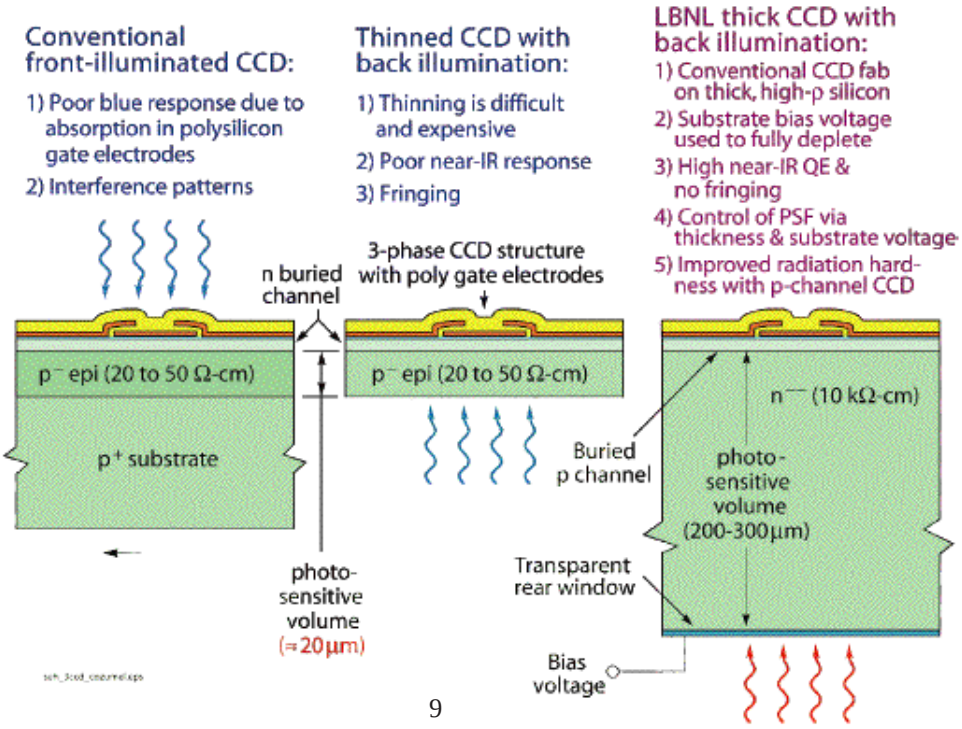

Figure 5: Three CCDs types cross-sections.

The cross-section on the right of Fig. 5 shows a conventional three-phase, triple polysilicon gate CCD with buried channel that it is fabricated on a high-resistivity n-type substrate. A bias voltage (substrate voltage) is applied to fully deplete the substrate, which is typically 200-300μm. The effect of this bias it is to remove mobile electrons from the extremely small number of phosphorous dopant atoms in silicon creating an electric field, due to the the dopant atoms that are ionized and positively charged. The field extends essentially all the way to the backside contact, depleting the volume of the CCD substrate. Fig. 6 shows the modeled, 2-dimensional potential field distribution within silicon. This potential in a fully depleted LBNL CCD directs the photon-generated carriers into the traditional potential wells formed by voltages on the frontside CCD gate electrodes resulting in minimal transverse diffusion of carriers. The resistivity, on the order of 10 kΩ/cm, allows for depletion depths of several hundreds μm. The donor density of the material, N_D is approximately (3.6-4.3)$\times 10^{11}$cm^{-3}. This high resistivity starting material allows for fully depleted operation at reasonable voltages,[1] and [7].

The backside has a 3-layer coating. The first layer is a very thin layer (10nm) of n^+ doped poly-Si used as an interface layer. The coating is followed by a layer of Indium Tin oxide (ITO). The top layer consist of 100 nm SiO_2. Both outer layers are transparent for UV/Vis light and thickness of the SiO_2 and the ITO was chosen to minimize reflection. The ITO layer is also used as electrode to apply the bias voltage, [1].

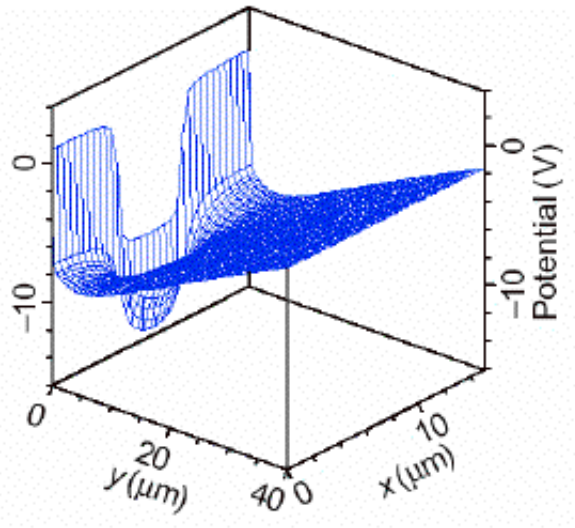

Figure 6: A 2D simulation showing the potential in a fully depleted LBNL CCD.

The choice of p-channel over the more conventional n-channel was due to the previous experience with fabrication of charged-particle p-i-n detectors, where it is found more straigthforward to produce low dark current devices. Unlike conventional CCDs the charge carriers are holes, not electrons. P-channel CCDs are presently under study for space applications due to the expected improvement in resistance to damaged produced by energy protons in the space environment [1].

The device schematic of a 2048×4096 pixel CCD is shown in Fig. 7. V and FS indicate the vertical and framestore parallel clocks in the imaging and storage areas respectively. In our case this last area is used as image area, typically connect FS1 to V1, ..., to read out the entire CCD. These CCDs have two readout transistors or two independent horizontal clock lines (H) that are labeled U and L respectively.

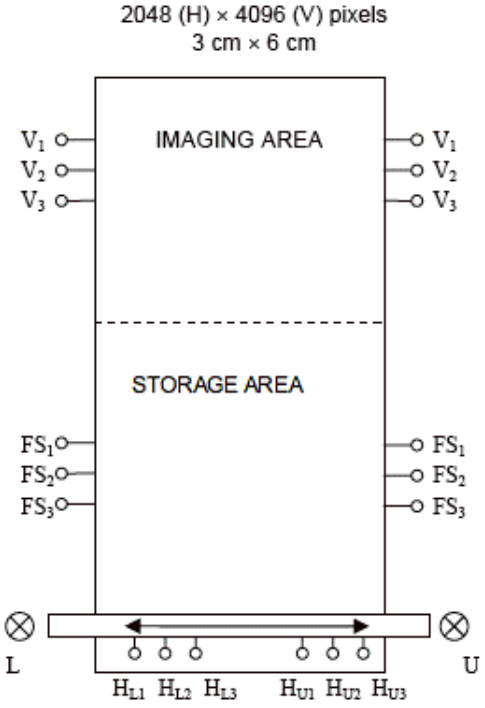

Figure 7: Device Schematic

The CCDs are packaged and tested at Fermilab, using the experience and infrastructure associated with the construction of silicon strip detectors for the Fermilab Tevatron program (see Ref.[9]). Early packaging effort emphasized construction of simple pictureframe-style modules. Six different pictureframe types have been assembled, allowing the testing of three different CCD sizes in either frontside or backside illuminated configurations. Fig. 8 shows all six pictureframe types. The window opening sizes and trace layouts correspond to the three different sensor sizes. The upper row is front side illuminated and the bottom row is backside illuminated.

The CCDs are held in place in the window opening by an aluminum nitride (AlN) ceramic support piece that is epoxied to the pictureframe board. AlN is a good match to silicon in thermal expansion coefficient and minimizes thermally induced distortions. These devices have been extremely useful for gaining experience with CCD handling and packaging and for development of the CCD testing facility.

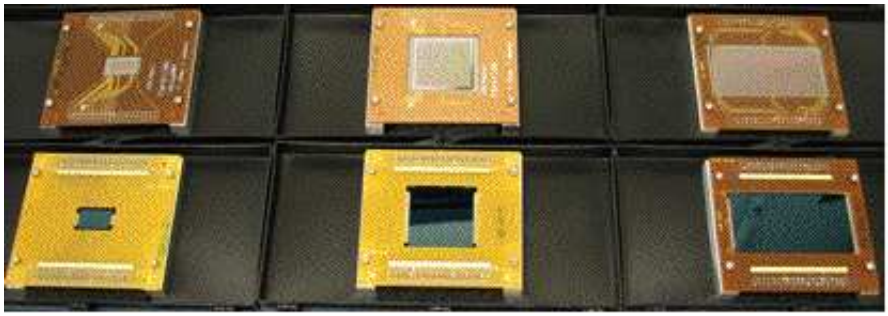

Figure 8: Six different pictureframe package types.

The packaging used in the focal plane will be a 4-side buttable package, called the pedestal package. The initial version of the pedestal package for the 2k$\times$4k devices builds on techniques developed by LBNL and Lick Observatory. Design of the packages for the guide and focus CCDs will follow the 2k$\times$4k development. Some CCD have been tested with this package until now.

The pedestal package consists of 4 main parts as shown in Fig. 9. The CCD itself is oriented with its backside, which has an antireflective coating, towards the incoming light. This face must be flat and have a uniform height relative to the modules mounting surface. A 37-pin Nanonics connector is located in the center of the device and is accessed through a hole in the foot. A temporary shorting plug is inserted into the connector.

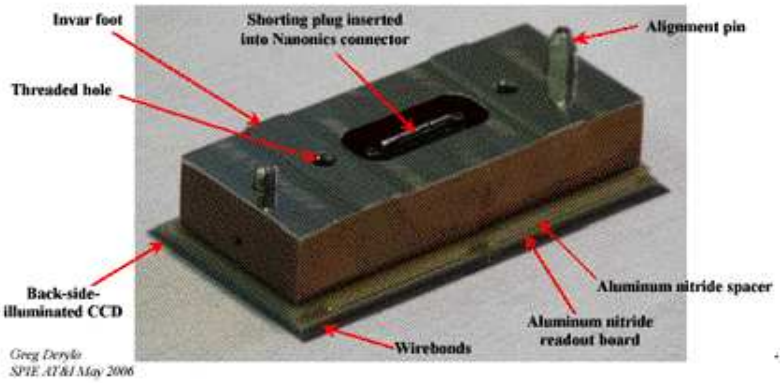

Figure 9: A complete pedestal package showing the CCD, the AlN readout board, the AlN spacer and the Invar foot

2.2 CCD Testing and Characterization. Measured Parameters.

Technically the CCD must perform four primary tasks in generating an image. The parameters or technical requirements to be measured in this document are classified within these four categories. These performance functions are called:

1. Charge Generation: the ability of a CCD to intercept an incoming photon and generate an electric charge.

2. Charge Collection: after the signal charge is generated, the CCD must be able to immediately collect it in individual pixels.

3. Charge Transfer: the ability of moving the charges to the output port accomplished by manipulating voltage on a parallel sequence of gates that form a CCD register.

4. Charge Measurement: the last major operation to occur during CCD imaging is to measure the charge collected in each pixel producing a digital signal.

Tab. 1 gives an overview of the tests performed in this work. They give which CCD functions are tested, what are the performance parameter used, the method or transfer curve use to test these performance parameters and finally the required specification for the performance parameters. In appendix A (see Sec. 7) the rest of the values used in the project are presented. In most cases, these values are similar to standard values in other CCDs. The exception is the quantum efficiency for which DES has a stronger requirement.

CCD Function	Performance Parameter	Transfer Curve or Test method	Specification
Charge Collection	Full Well Capacity	Photon Transfer	> 130000 e^-
Charge Transfer	Charge Transfer Efficiency (CTE)	X-Ray and EPER method	> 0.99999
Charge Measurement	nonlinearity	Photon Transfer	< 1 %
	readout noise	Photon Transfer	$\leq$ 15 e^-/pix

Table 1: CCD specifications

2.3 Testing Procedures in the Production Phase.

The complete suite of test comprise three stages. The first stage is performed on every packaged CCDs and takes approximately one day. CCDs are discarded as they fail to pass a testing stage in this process. At the peak of production at FNAL, four CCDs will be tested per week. The testing stages are summarized below and will be described in more detail in Sec. 4. An alternative method with a x-ray source for calibration and CTI calculation is also described.

Testing Stage 1

1A. Photon Transfer Curve.

The photon transfer curve is obtained for each CCD. We compute the gain, linearity, full well capacity and readout noise from it.

1B. Clock Rail Scan

The clock rail scan is performed to verify the technical requirement on charge transfer inefficiency (CTI). Each of the four clock rails (horizontal upper and lower rail, vertical upper and lower rail) used for the charge transfer between pixels is varied.

1C. Output Gate Transfer

The goal is to measure the voltage at which charge injection is produced in the device as a function of V_{ref} (reset drain voltage).

These measurements allow us to confirm that the operating bias voltages chosen make sense and to learn how the performance of the detectors changes when the bias voltages vary.

1D. Charge Pumping

Charge pumping studies will be done for each device with the objective of detecting low level traps in our detector which will comply with the technical requirement TD.16. The number of pumped lines will be varied as well as the illumination levels.

1E. Dark and Flat Exposures

These data will be used for quantifying cosmetic defects.

Testing Stage 2

2A. Quantum Efficiency Measurements

The QE measurement will be done using a 6 position filter wheel and will measure the absolute QE with a precision of 10% for the narrow band filters centered at 400, 500, 600, 800, 900, 1000 nm. A set of dark and flat exposures is taken for each filter position, producing a total of 12 exposures. This step is done to verify TD.7.

2B. Charge diffusion Measurement

The current plan includes a charge diffusion measurement for each CCD that passes all other tests. This measurement is done to certify the technical requirement TD.13. The diffusion will be measured as a function of substrate voltage (V_{sub}).

2C. Temperature Scans

Once all the other tests are performed on the CCD, we will measure the QE at 1000nm and the dark current levels as a function of temperature. These data will be used to certify TD.8, TD.10 and TP1.

The device is removed from the CCD testing station after the Stage 1 and 2 tests. The CCD could then be transferred to a flatness measurement station for Stage 3 Testing.

Stage 3 Testing

3A. Flatness measurement

Including cool-down and warm up, the test is the 2 to 3 days long. In order to understand the need for this test in the future, we plan to accumulate data on flatness for science packages which fail to readout. If needed, a measurement of flatness on each CCD could be done.

3 The Test Bench Set Up

3.1 Overview

In order to acomplish the CCD testing goals a device testing facility was built at Fermilab. For the purpose of CCD testing a special area of the Silicon Detector (SiDet) facility at Fermilab was adapted for CCD operation. This includes controlled high humidity (> 40%), extensive Electrostatics Discharge (ESD) safety equipment and automated LN_2 supply.

The group Barcelona is in charge of some modifications of the front end electronics to read the camera and collaborates in testing the CCDs with Fermilab. The group is modifying the Master Control Board of the Monsoon readout system to make it accessible through an S-LINK optical fiber connection and a new Transition Board for the Clock Board. A cryostat to test the electronic boards with a CCD inside it at cryogenic temperature was also built. The optical and electronic equipment to do the electronic test that are explained in section 4 was developed. Give that the first goal at Barcelona is to test the new boards there are fewer requirements in the laboratory than at Fermilab although it is provided of ESD safety equipment. Latter on there will be a clean room with controlled humidity and extensive ESD safety equipment to develop a laboratory to characterize CCDs.

The temperature operating of the CCD is determined by the QE and dark counts requirements. The QE increases with temperature especially at long wavelengths while the dark counts decreases. The survey requirements on dark counts are achieved for temperatures lower than 180 K. The current studies carried out at Fermilab show that a good compromise is reached at a temperature of 173 K, see Ref.[5].

When the test started at Barcelona the best operating temperature had been not defined yet. For our first tests explained here the operating temperature was 160 K. Currently we are operating at 173 K.

The low operating temperature of the CCD require the use of a cryostat to hold them and maintain them cold. The cryostat built at Barcelona was design to be able to hold CCD of differents sizes, 2k$\times$4k, 2k$\times$2k and 0.5k$\times$1k to allow flexibility of tests.

The general sketch of the test bench is given in Fig. 10. The main system architecture is derived from the Quantum Efficiency test setups of the SNAP group and the ESO group. The list of parts is in Sec.8.

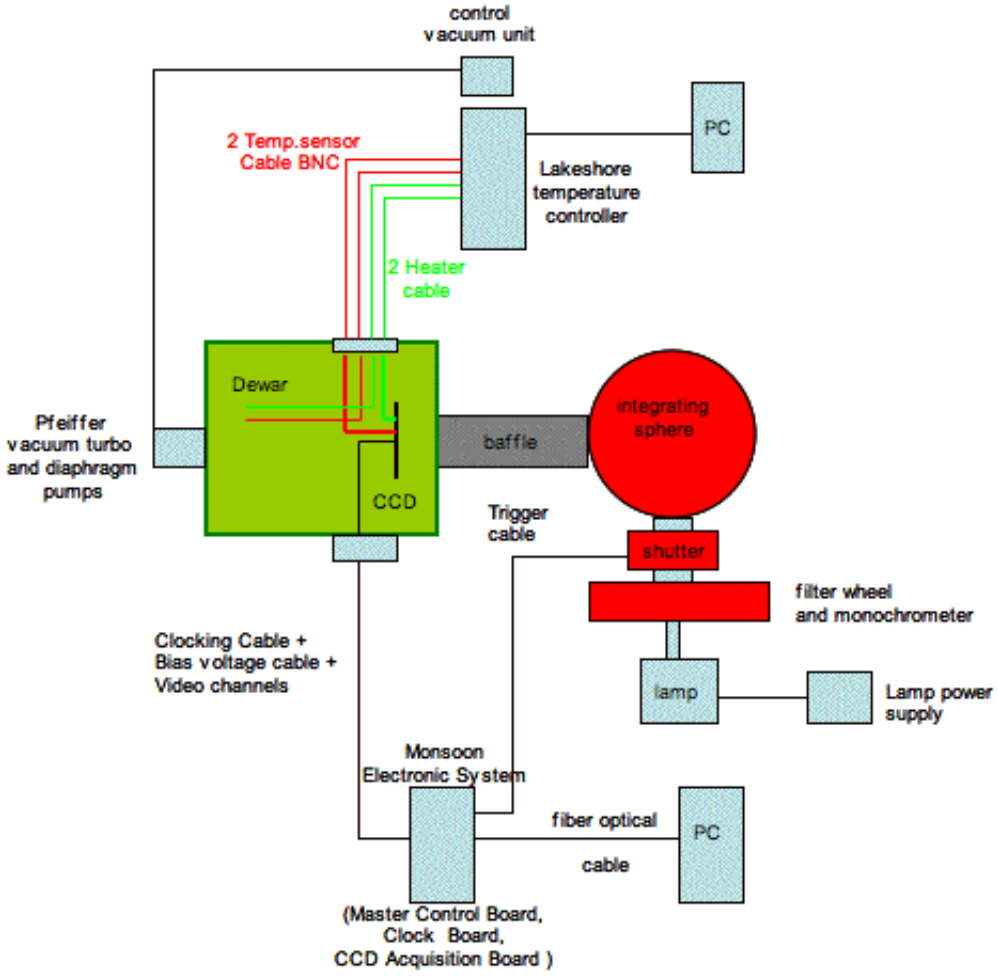

Figure 10: Test bench for electronic test.

3.2 CCD testing dewars

Five cryostats at Fermilab and one at Barcelona like the one shown in Fig. 12 have been built. The dewars are cooled with LN_2 and can be controlled to maintain a stable temperature using proportional-integral-derivative (PID) loops.

The design of the dewar shown in Fig. 12 allows for a quick exchange of CCDs which is a very important ingredient for the rate of testing that it is needed for this project. The dewar has manual clamps that can be loosened by hand and give clear access to the front, where the CCD is installed. Typically, once a CCD is loaded in

the dewar it takes about 1 hour to produce a vacuum better than 2×10^{-5} mbar or Torr. This is important to ensure no contaminant freezes onto the CCD. At this point LN_2 can be loaded and approximately 2 hours later the stable operating conditions at 160 K are achieved. Fig. 11 shows a general sketch of the system.

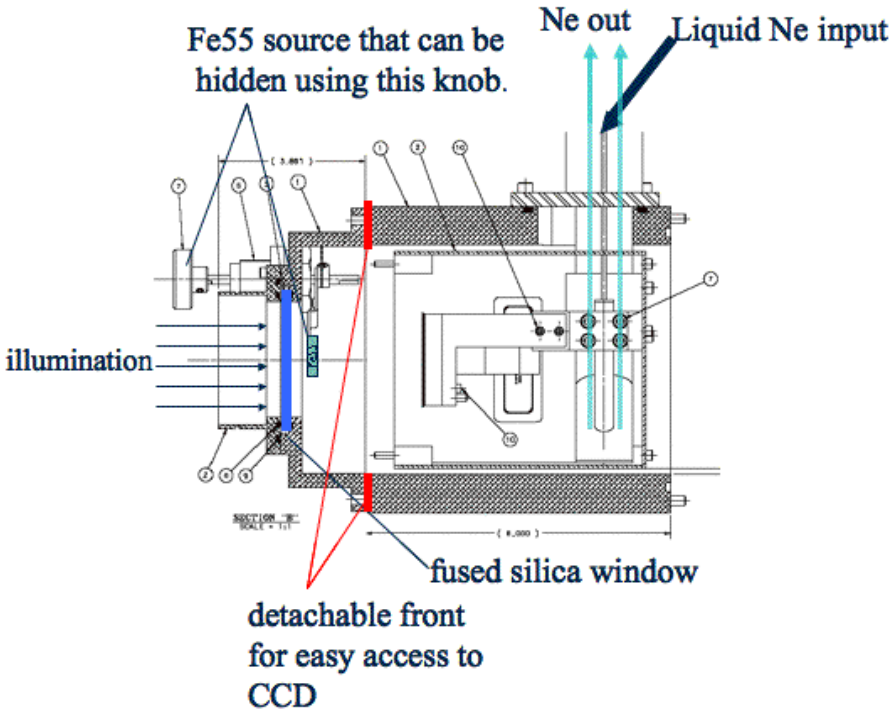

Figure 11: General view of the cubes

Liquid nitrogen LN_2 is introduced from the top. The front window allows the complete illumination of a 6×3 cm area which corresponds to a 4096×2048 pixel CCD for our pixel size. The exterior walls of the dewar are made of aluminum and inside there is a Cu box that isolates the cold parts from the exterior walls. The front cover is removed and the CCD is mounted inside in a picture frame or in a pedestal package.

Fig. 15 shows a front view drawing of the cryostat without the cold plate and the cold finger. The small diameter tube is used to vent the evaporated nitrogen. A valve outside is used to control the flow of gas, setting in this way the level of LN_2 inside the dewar. The bigger diameter tube is used to fill it with LN_2. The CCD is placed on the cold plate and is cooled by thermal diffusion through the cold finger, as Fig. 16 shows.

Figure 12: Dewar fully assembled

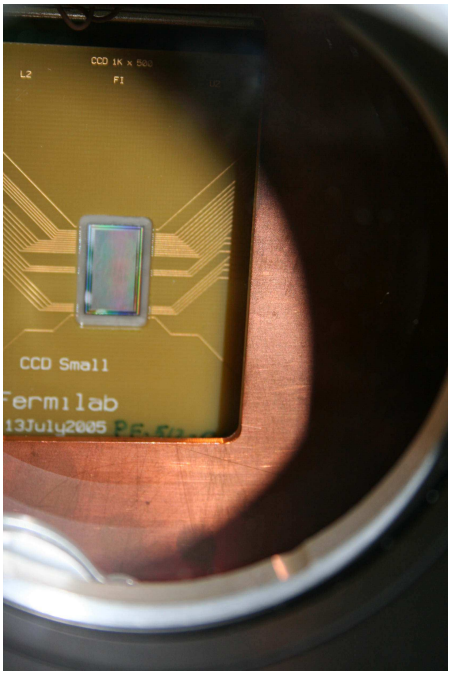

Figure 13: 512×1024 CCD illumination

Figure 14: Dewar without front cover.

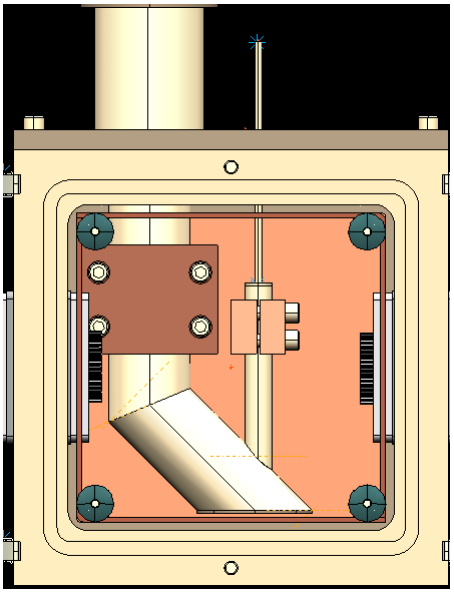

Figure 15: Inner cube

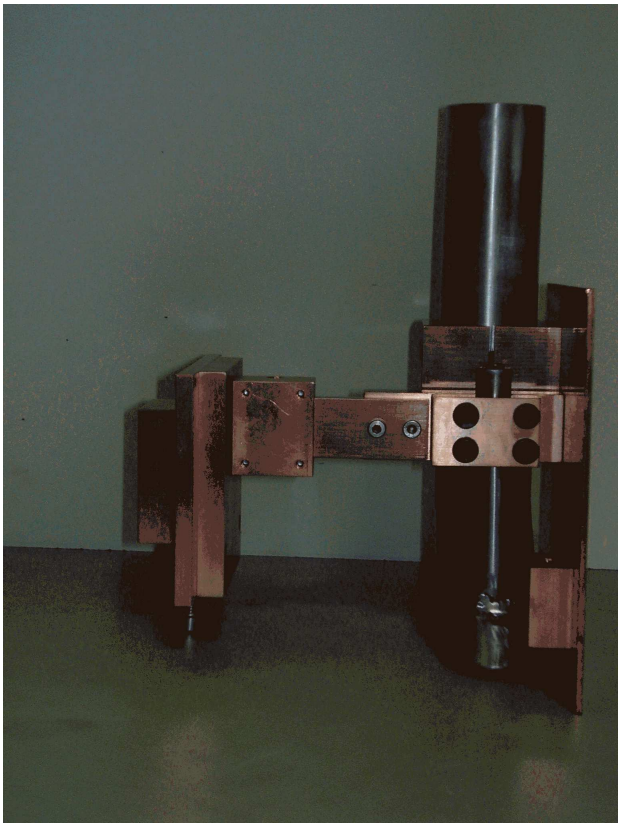

Figure 16: Cold finger and cold plate before install inside the cube

3.3 Cryogenics and Vacuum

A desired vacuum pressure of 2×10^{-5} Torr or mbar is required in the cube to prevent the contaminant to freeze onto the CCD. In order to achieved that, a turbomolecular pump and a diaphragm pump as backing pump are used to remove most of the gas. Once the ultimate pressure is achieved LN_2 is poured in the deposit and the cryo pump takes over to start the cooling while the rest of the pumps are still on. The cryo pump will also remove the water that is the majority gas load and the pressure will decrease down to approximately 1×10^{-6} Torr. See Fig. 17. Note that the pressure scale is logarithmic and the temperature is linear.

The turbo pump has a speed of 33 l/s but the effective value is reduced due to conductance of the connection system. The total time to achieve the ultimate pressure is approximately one hour.

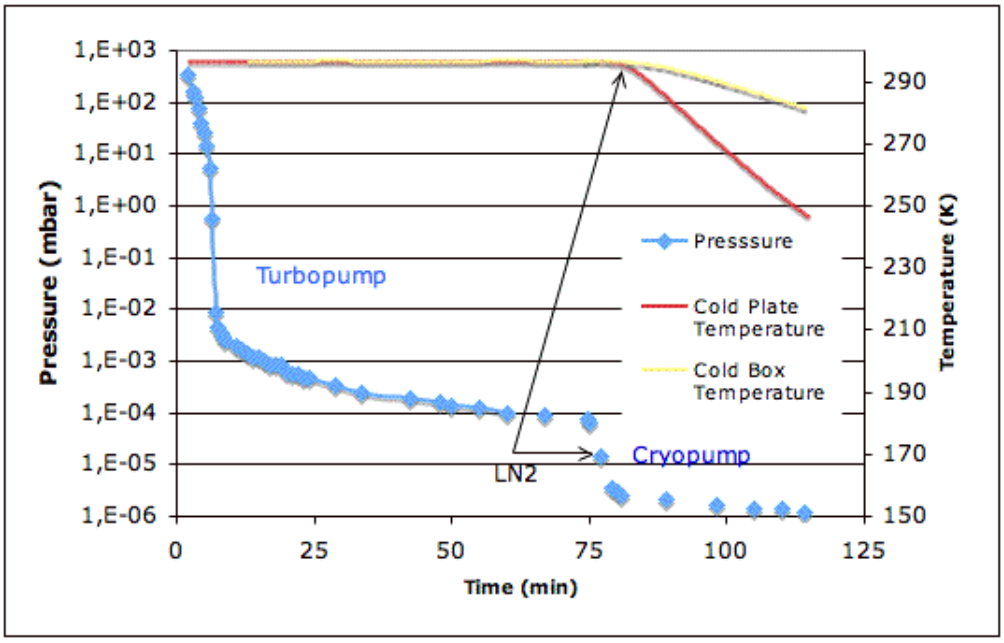

Figure 17: Pressure plot as a function of time and type of pumping.

At Barcelona the turbopump is separated from the diaphragm pump and it is put at the back cover of the cube through a flexible hose of 0.25 m to avoid vibrations and minimize the leak of the conductance because this last variable decreases with the lenght of the pipe (see Fig. 18). Above the turbo pump there are a vacuum gauge and a safety relief valve in case of a leak of LN_2 inside the cryostat . A Display Control Unit is connected to the vacuum gauge and turbo pump to control them and measure the vacuum values.

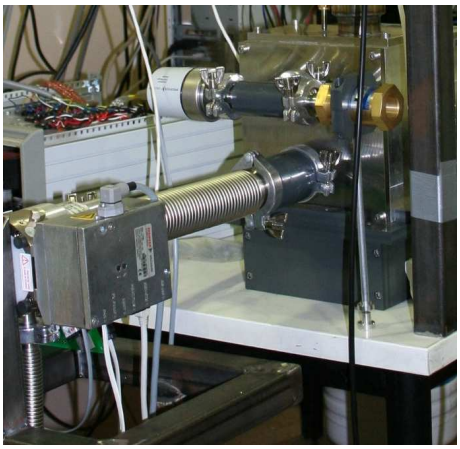

Figure 18: Vacuum system at the back of the cube.

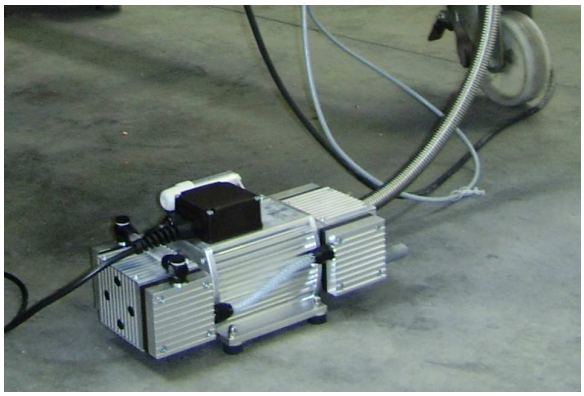

Figure 19: Diaphragm pump and hose that connects with the turbo pump.

The QE at high wavelengthts is very dependent on temperature as the QE stability studies made at Fermilab show. To fulfill the requirement T-21 (QE instability less than 0.3% in 12-18 hours) is need a temperature stability of 1 K in the focal plane.

The Lakeshore temperature controller is used to maintain at a fixed point the temperature of the cold plate where the CCD is. An independent, proportional-integral-derivative (PID) control algorithm calculates the control output of the heater power based on a temperature set point and feedback from the control sensor. The autotunning feature of the model automates the tuning process in our system, although it can be set manually to achieve better results and smaller fluctuations. In our system at 160 K fluctuations below 1K are achieved with the autotunning system, see Fig. 20. As long as the cooling system is operating the temperature of both sensors will approximate and reduce the fluctuations.

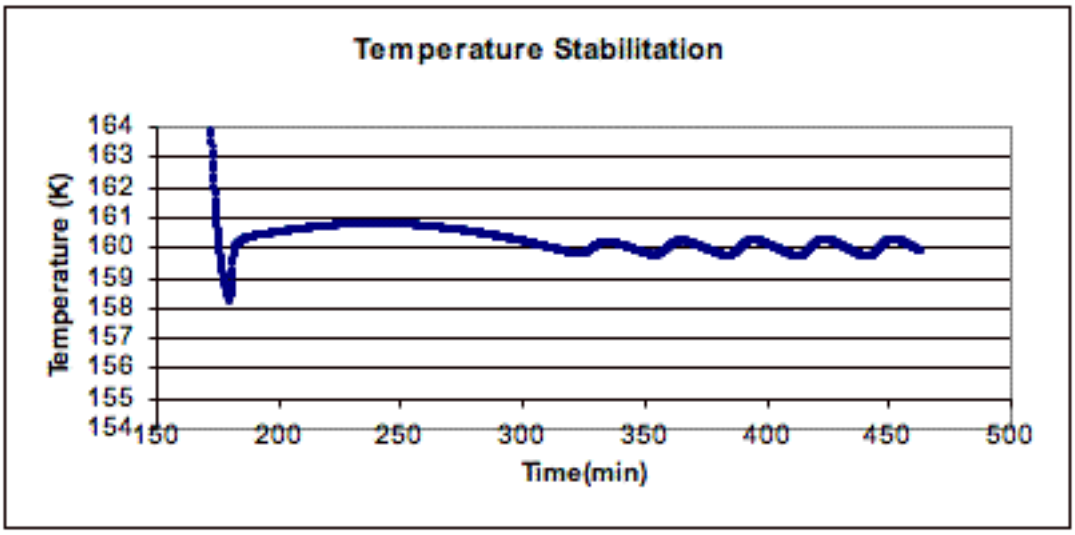

Figure 20: Temperature stabilization of cold plate at 160 K with PID automatically.

Fig. 21 shows the position of the temperature sensor and the heater for the control loop (green rectangles are the heaters and the red squares are the sensors). The other sensor is used to monitor the cold box temperature and the other heater is used to heat the system in case of forced warm up before turning off the vacuum pump. Note that the monitor sensor would be more useful if placed close to the vent tube to know the temperature of the colder part of the cube and to study the temperature equilibrium of the copper arm. The temperature of the two places will approximate and be equal when this equilibrium is reached. This is because of the thermal conductance of heat along the vent tube and the cold plate.

The controller has two control loops but only the first is used to stabilize the temperature. The two heaters are put inside a copper box and have a resistance of 25 Ω. The loop 1 has three ranges, two of them for low cooling power. For a given I, V and R values the power is the minimum following the Eq. 1. The maximum power they provide is 25 W in the higher range as they feature a maximum current of 1 A and a heater output compliance of 50 V.

$$P = I^2 R = V^2/R \tag{1}$$

In our system the minimum range is needed to stabilize the temperature given a maximum power of 250mW. The second loop is a single range, variable DC voltage that varies from 0 V to 10 V, but it is used as a voltage source for the heater instead of using it to control the temperature. The output can source up to 1 A of current providing a maximum of 4 W for heating. In order to warm the cold box faster the heater can be switched to the loop 1 that provides more maximum power than the second.

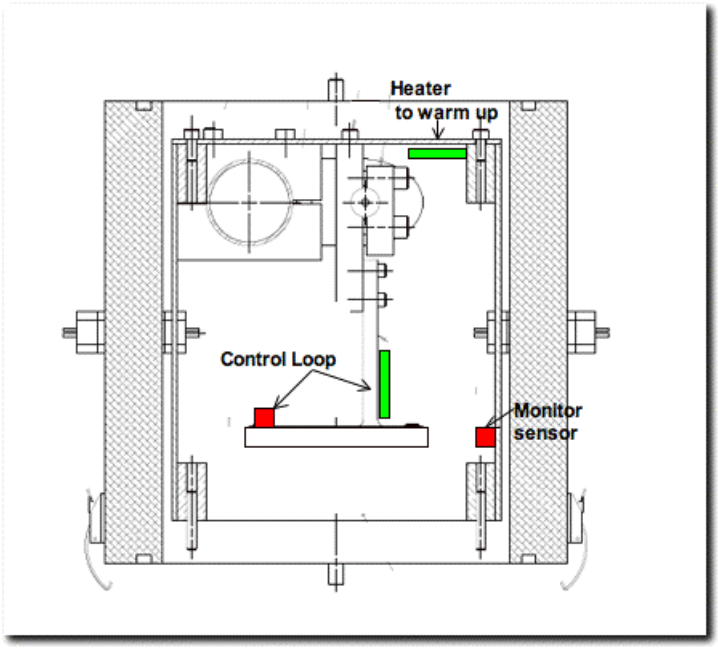

Figure 21: Cryogenic system.

The temperature sensors installed are temperature diodes. The are based on the temperature dependence of the forward voltage across a p-n junction and can be used from 1.4 K to 500 K. From 25 K to 500 K they have a nearly constant sensitivity of 2.3 mV/K. The sensors are mounted in a special semiconductor package easy to install with a screw head. These sensors follow a known standard response within a given tolerance so it was not neccesary to calibrate them because a calibration data curve is provided with the controller. Silicon diode sensors typically excite with a constant 10μA current and their output is fairly large: 1 V at 77 K and 0.5 V at room temperature.

Note that sensors have an accuracy of 1.5 K or 15% depending on the temperature range. However such sensors will not be used in the scientific package to know exactly the CCD temperature. They are only used in the early test set up with the picture frame package.

The wire used for the heater is made of copper but for the sensor phosphor bronze is used because has lower thermal conductivity that helps minimize the heat flow through the leads in the sensor.

When the system is warm up can not be opened until its temperature reaches the dew point.

The temperature stabilization is controlled by a Labview program that also collects the temperature and the heater power data.

3.4 Electronics

Figure 22: Monsoon Readout System with S-Link and 8-Channel ACQ Board.

The CCD readout is based upon the Monsoon system; this includes the software running in a PC under a Linux operating system, a DHE Monsoon crate with the Master Control Board (MCB), the Clock Board (CB) and the CCD Acquisition Board. Monsoon is a very flexible system specifically designed for controlling large mosaic arrays. To achieve the low noise specifications given changes to the production version of Monsoon are being made but the detailed studies are not presented in this work.

The MCB is the system interface. It controls all backplane functions, such as reading and writing to registers, as well as controlling the readout of the CCDs. Through an optical fiber interface cable, it communicates with a host computer. This communication link is currently based at Fermilab on mezzanine cards (Systran FibreXtreme SL100/SL240 Series) which exist on the MCB and in the host computer. Some concerns arose over the long term support and availability of the Systran product: therefore, work is underway in Barcelona to replace the present Systran link with S-Link. S-Link is a well known open-source communication link also used in CERN experiments.

The second type of Monsoon board being used in the CCD characterization tests is the 8-channel CCD Acquisition Board (ACQ8). This board currently provides eight channels to digitize the CCD video outputs as well as 32 bias voltages. In reviewing this board, a redesign would create to reduce the number of overall boards required

by the telescope system. Thus, a new design of 12-Channel CCD Acquisition Board is being tested at Fermilab. Note that the data taken for this work were taken with the 8-channel board. This new board will provide for the readout of 12 CCD video outputs, the readout of the Resistance Temperature Detectors (RTDs) incorporated in the CCD packaging, automatic control required for the erase mechanism, and the bias voltage for the 6 CCDs readout.

The third type of Monsoon Board is the Clock Board (CB). This board was re-designed to provide many more clock outputs and therefore was service to nine CCDs. This last modified board is still under development thus the first CB is used in this work.

3.5 Optical equipment

The optical setup described is designed to provide flat field images for tests that are explained in section 4. The setup design in Barcelona and Fermilab are equal but with different models of optical instrumentation. It includes a light source, a monochromator with a filter wheel, a shutter that controls the exposure time, a 6" integration sphere that provides a uniform, parallel beam of normal incident light in the detector and a baffle to propagate the light to the front cover of the CCD. Studies made at Fermilab show that the uniformity of illumination varies a maximum of 2.2 % over 6 cm transverse to the light source at a distance of 13 inches from the source and a maximum of 10.3 % at 7 inches. Therefore the distance selected between the CCD and the output port of the sphere is 13 inches. This setup is in the first stage because more optical studies are needed to measure the quantum efficiency and diffusion as is doing at Fermilab and in Barcelona.

3.6 Data Collecting

The images for the CCD characterization are automatically collected using Tcl/Tk based software that communicates with the Monsoon Pixel Acquisition Node (PAN) via network sockets. This allows the user to implement any sequence of exposures. A metadata file is produced with the information for each image (voltage setting, exposure time, etc).

4 CCD Testing and Characterization

4.1 CCD performance. Output Transfer Gate Transfer

The operation of astronomical CCDs require the application of voltages according to generated clock signals. Their characteristics determine the performance of the CCD in term of how charge is collected, transferred and measured (see section 2.2). For our thick CCDs fabricated on high resistivity silicon, we have the advantage that we can vary the clock signals to optimize the performance of some parameters while the nearly independent substrate bias id used to achieve full depletion.

Given the importance of voltages and clock settings, we perform a test to determine their optimal values prior to performing the characterization experiments to check the fulfillment of the technical requirements. In our case all the operating voltages are given by LBLN, see Tab.2, so this test is not strictly necessary and does not address any specific technical requirement. These measurements allow us to confirm that the operating voltages chosen make sense and to study how the performance of the detectors changes when the bias voltages vary.

We begin this section by introducing CCD theory in the subsection 4.1.1. Then in section 4.1.2 we explain in detail how we determine the channel potential inside the CCD under the output gate.

In short, the sense node or output diode is the region where the signal is dumped from the horizontal register allowing the measurement of the charge packet size as a voltage. The goal is to measure the voltage at which charge is injected from this region into the serial (horizontal) register of the device as a function of V_{ref} (reset drain voltage). The injection is controlled by the output gate. This technique allows the determination of the channel potential inside the CCD under the output gate and it will be explained in detail in subsection 4.1.2.

Signal	**Signal Name**	**Typical Voltages**
Substrate Bias	V_{sub}	40 V
Output Drain	V_{dd}	-22 V
Reset Drain	V_{ref}	-12V
Output Gate	V_{otg}	3.5 V
Vertical Clocks	V1, V2, V3	+5.5 V, -2.5 V, 5.5+V
Horizontal Clocks	H1, H2, H3	+8.5 V, -3.5 V, 8.5 V
Transfer Gate	Tg	+5.5 V, -2.5 V
Summing Well	SW	-4 V

Table 2: LBNL CCD operational voltages.

4.1.1 Introduction: Potential for an overdepleted CCD. The Buried-Channel Potential Well. Depletion and Charge Injection.

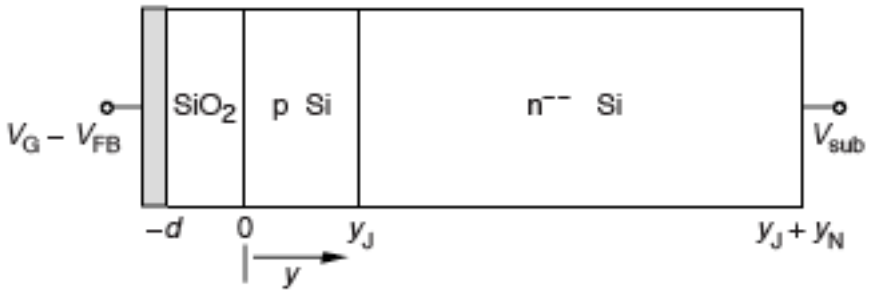

Figure 23: CCD cross section.

Fig. 23 shows the cross-section of the p-channel back illuminated CCD. The gate insulator thickness is d, the junction depth is at y_J, and the thickness of the substrate is $y_J + y_N$. A one dimensional depletion-approximation solution to the Poisson equation for a thick CCD with applied substrate bias is given in Ref.[1]. The potential V_J at the buried-channel/substrate junction is approximately equal to the potential minimum and is given by

$$V_J \approx V_G - V_{FB} - \frac{qN_A}{2\varepsilon_{Si}} y_J^2 (1 + \frac{2\epsilon_{Si} d}{\epsilon_{Sio_2} y_J}) \tag{2}$$

which is independent of the substrate bias voltage. V_G is the applied gate voltage, V_{FB} is the flat-band voltage associate with fixed charge in the oxide layer, q the electron charge, N_A is the doping density in the p-channel of depth y_J, d is the gate insulator thickness, ϵ_{Si} and ϵ_{SiO_2} are the permittivities of silicon and silicon dioxide, respectively. The third and fourth terms of equation 2 are the voltage drops across the fully depleted channel and the voltage drop across the oxide when the channel is fully depleted. This equation is valid for $N_D \ll N_A$ and $y_N \gg y_J + (\epsilon_{Si}/\epsilon_{SiO_2})d$ as in our CCDs. Equation 2 is a one-dimensional approximation to a decidedly two-dimensional problem. Fig. 24 shows how the effect of the barrier phases slightly raises the value of V_J when compared to the 1-D approximation. However, it is still true that the potential at the junction is a weak function of the substrate bias due to the large difference in doping between the channel and substrate and the use of a thick depleted substrate.

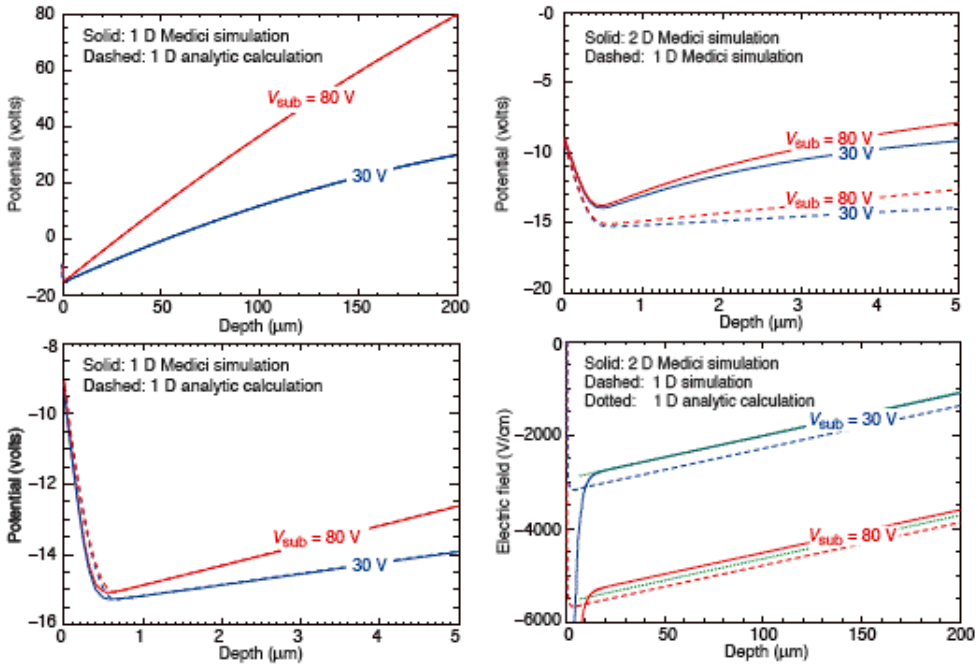

Figure 24: Left: Calculated and simulated 1D potential versus depth for a CCD operated in overdepletion. Bottom right: Calculated and simulated electric field versus depth. Top right: 2D and 1D simulation for different values of V_{sub}

The p-buried channel must be completely depleted of majority carriers (holes) to distinguish them from signal holes when generated.

The buried-channel can be thought of as an n-p junction with a gate and insulator (SiO_2) at the exterior surface of the p-side, see Fig. 23 and Fig. 25. Two depletion regions are created. One depletion region is formed around the n-p junction when the detector is biased with a reference voltage V_{ref}, and the second one appears at the surface in the p-material as uncompensated acceptor ions when a voltage V_{otg} (or V_G in Fig. 25) is applied to the gate. If the latter voltage is positive relatively to the channel potential the holes will be repelled away from the surface. These negative lattice charges induced by the gate cause the potential in the p-material to increase abruptly as the surface is approached.

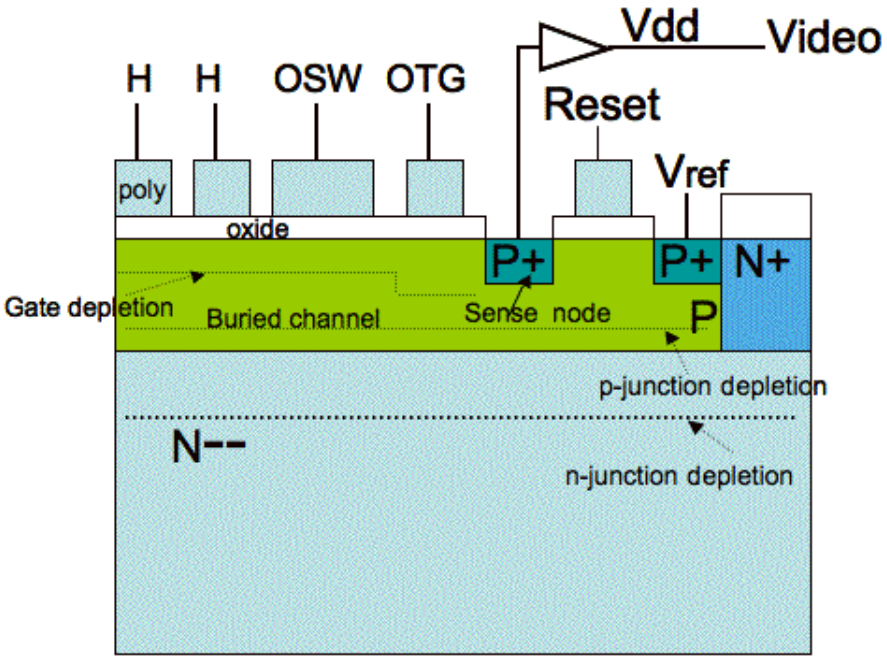

Figure 25: CCD cross section of output region showing gate and n-p junction depletion region.

For a fixed gate voltage, a V_{ref} will be reached for which the two depletion merge into one, extending from the surface completely throught the p-material and deep into the n material. The point where the two depletion regions meet in the buried channel is where the minimum channel potential V_{min} is locally found. The potential is exactly equal to V_{ref} when the two regions merge. V_{ref} is connected, through the reset switch, to the output diode or sense node which is embedded in the p-buried channel.

Depletion must first take place under the output transfer gate before the other phases of the array can be depleted of the majority carriers. Once the output transfer gate is depleted, the output summing well and the horizontal and vertical registers can be depleted simply by clocking them.

As long as the channel potential under the output transfer gate is higher than the reference voltage, holes from the sense node will see a barrier and not move backward into the array. Charge injection occurs when the channel potential under the output transfer gate becomes equal to V_{ref}.

4.1.2 Effective Threshold. The Output Transfer Gate Transfer curve. Experimental Results

The effective threshold, V_{eff}, is one of the most important parameters measured when characterizing CCDs. The relationship between the applied transfer gate voltage V_{OTG} (V_{otg}) and the channel minimum potential V_{min} when full p-channel depletion has been established is:

$$V_{eff} = V_{min} - V_{OTG} \tag{3}$$

This parameter can be readily measured from an important transfer curve called the Output Transfer Gate Transfer, see Fig. 26. This curve plots V_{ref} as a function of V_{OTG} for those points where the charge injection takes place. The injection can be reached by decreasing V_{OTG} or increasing V_{ref}. The results show that the voltages are satisfactory because the operating point it is away from the charge injection region.

The charge injection break point defines V_{eff} through the equation

$$V_{eff} = V_{ref} - V_{\frac{OTG}{CI}} \tag{4}$$

where $V_{\frac{OTG}{CI}}$ is the output transfer gate voltage when injection takes place and obeying that $V_{min} = V_{ref}$ when this effect occurs.

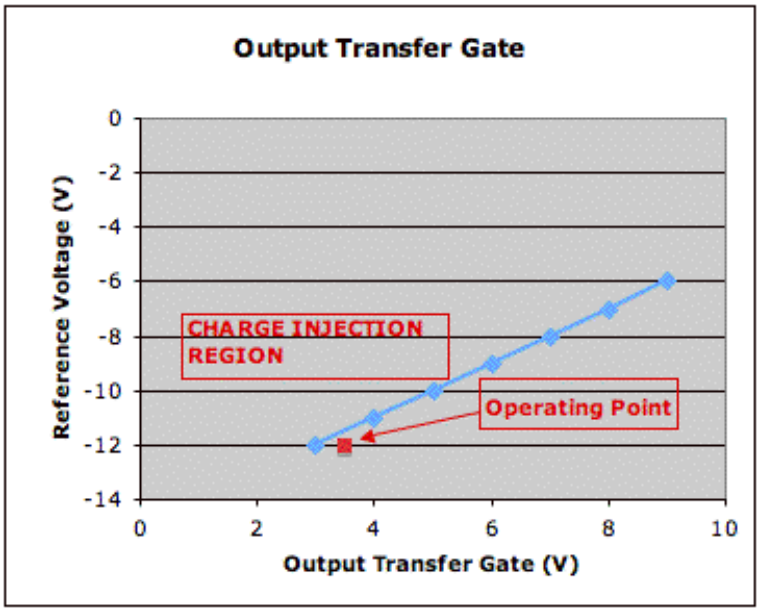

Figure 26: Output transfer Gate Transfer curve that shows charge injection region and the operation point.

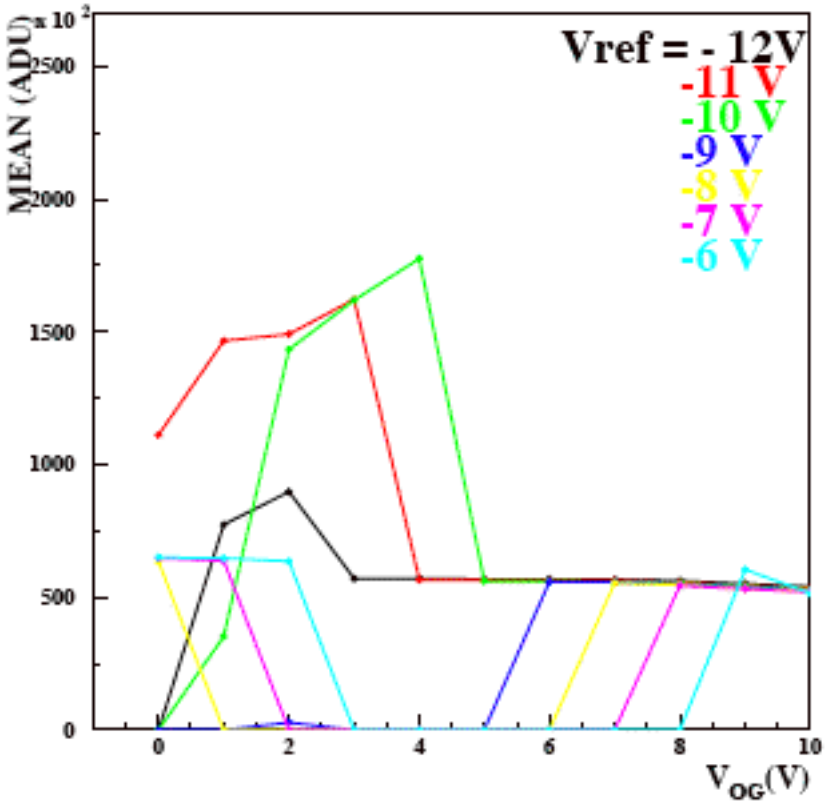

Figure 27: Output transfer gate voltage require to cause charge injection for different V_{ref} .

The Fig. 27 shows the mean value of the signal measured in the overscan area of 100$\times$ 400 pixels as a function of V_{OTG} for different values of V_{ref}. When charge injection is produced large deviation from pedestal values are seen. The breakpoints seen in this figure are used to generate the Output Transfer Gate Transfer curve in Fig. 26. The data are taken from the back illuminated 2k$\times$4k CCD called s1-11 CCD at Fermilab. The errors bar are calculated but are small to be seen in this scale. The high decrease of the mean to zero at $V_{ref} \geq -9V$ is due to the saturation of the ADC.

Taking the black line that corresponds to V_{ref} = -12 V and $V_{\frac{OTG}{CI}}$ = 3V, the effective threshold voltage is

$$V_{eff} = V_{ref} - V_{\frac{OTG}{CI}} = -12 - 3 = -15V$$

The V_{eff} is a constant because of the linear relationship between V_{ref} and V_{OTG}, as can be seen directly measuring V_eff as a function of increasing V_ref values.

This conclusion it is probed looking at curves taken increasing the V_{ref} values. These results show that when $V_{OTG} < V_{ref} + 15V$ charge injection takes place.

4.2 Photon Transfer

The photon transfer technique is one of the most valuable tools for calibrating, characterizing, and optimizing performance. It is used to evaluate numerous CCD parameters in absolute terms. These parameters include full well capacity, linearity, pixel no uniformity, readout noise, dark current, quantum yield, sensitivity, signal-to-noise ratio, offset and dynamic range. In the next subsection, some of these parameters are explained and measured. This is usually the first test performed in determining the overall health of a new CCD system, because all the hardware and software must be in perfect operating order. The photon transfer curve also gives the constant used to convert relative digital numbers generated by the camera into absolute physical units of electrons. This very important conversion constant is referred to as the 'camera gain constant', expressed in e^{-}/ADU. The section 4.2.5 will show how the photon transfer curves are generated and how the constant is found.

4.2.1 Photon Transfer Derivation

The schematic representation of a typical CCD camera is shown in Fig. 28. There are five transfer functions, three are related to the CCD (interacting QE, quantum yield and sensitivity of the sense node of the output amplifier) and two associated with the off-chip signal processing circuitry (signal chain gain and ADC gain). The input of the camera is given in units of incidents photons and the final output is achieved by encoding each pixel signal into a digital number S(ADU) that in the case of the DES camera is 18 bits wide.

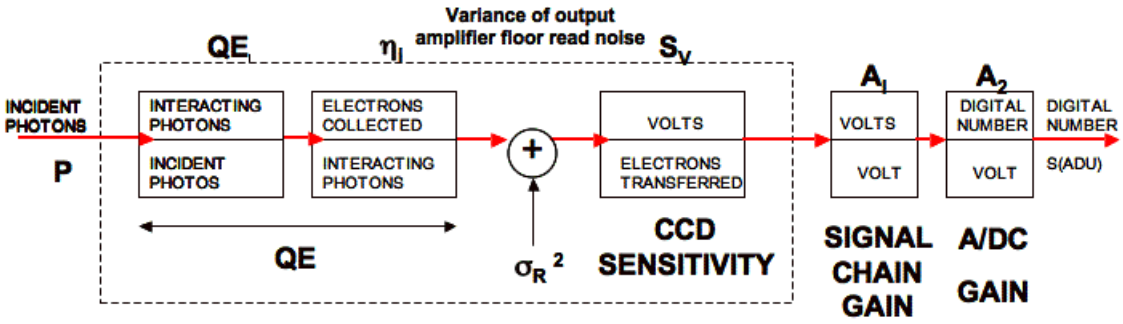

Figure 28: CCD camera scheme.

The output signal S(ADU) that results for a given exposure period is given by:

$$S(ADU) \quad = \quad PQE_I\eta_i S_v A_{CCD} A_1 A_2 \tag{5}$$

where P is the average number of incident photons per pixel, QE_I the interacting photons per incident photon, η_i is the quantum yield or number of electrons generated, collected and transferred per interacting photon, S_v is the sensitivity of the sense node (V/e$^-$), A_{CCD} is the output amplifier gain (V/V), A_1 is the gain of the signal processor (V/V) and A_2 is the gain of the ADC (ADU/V).

To convert the output signal ADUs into fundamental physical units, it is necessary to find the appropriate conversion factor. The photons with wavelengths longer than 400 nm generate single $e^- - h^+$ pairs, so the quantum yield for our light range is $\eta_i = 1$. Assuming a unity quantum yield, the Eq. 5 can be written as

$$S(ADU) = PQE_I/K = P_I/K \tag{6}$$

where P_I is the number of interacting photons per pixel ($P_I = QE_IP$) and $1/K = S_v A_{CCD} A_1 A_2$

The constant K can now be determined by relating the output signal to its variance, σ^2. The variance of Eq.6 is found using the propagation of errors formula,

$$\sigma_S^2(ADU) = \left[\frac{\partial S(ADU)}{\partial P_I}\right]^2 (\sigma_{P_I}^2) + \left[\frac{\partial S(ADU)}{\partial K}\right]^2 (\sigma_K^2) + \sigma_R^2(ADU) \tag{7}$$

where the variance is added of the output amplifier read noise floor $\sigma_R^2(ADU)$.

Performing the required differentiation on Eq.7 and assuming that the constant K has a negligible variance (i.e. $\sigma_K^2 \simeq 0$), the variance in $S(ADU)$ is :

$$\sigma_S^2(ADU) = (\sigma_{PI}/K)^2 + \sigma_R^2 \tag{8}$$

Using $\sigma_{P_I}^2 = P_I$ (photon statistics, Poisson) and Eq.7, the important expression to convert output noise and signal measurements in ADU directly into units of electrons is

$$K = \frac{S(ADU)}{\sigma_S^2(ADU) - \sigma_R^2(ADU)} \tag{9}$$

where K is the camera gain constant measured in e^-/ADU.

Assuming that read noise is also negligible ($\sigma_R(ADU) \ll \sigma_S$)

$$K = \frac{S(ADU)}{\sigma_S^2} \tag{10}$$

4.2.2 Photon Transfer Curve and Calculation of Gain

The photon transfer curve is the response of a CCD that is uniformly illuminated at different levels of light. It is obtained for each CCD by setting the operating voltages to the default values and taking pairs of flat fields for each exposure time. The exposure time is increased and the signal level is measured in ADUs until saturation is reached. The exposure time is the period when the shutter is opened or the CCD is exposed to the light source. This is the standard procedure to obtain the gain for a device assuming a fixed electronic noise and poisson statistics for the number of photons as described above.

The Pixel Response Non Uniformity (PRNU) noise results from sensitivity differences among pixels. Fabrication problems generate pixels with different responsivities. The shot noise associated with random arrival of photons follow Poisson statistics, however the PRNU noise is not governed by this statistics and is eliminated by simply subtracting, pixel by pixel, two images taken one after the other at the same exposure level. The assumption that the Poisson noise of the flat field photons themselves σ_{P_I}, is much greater than the read noise floor, σ_R is made too.

The photon transfer curve plots the variance of the measured ADUs as a function of the exposure time:

- Variance data $\sigma^2(ADU)$ on the ordinate axis are found by calculating the variance of an area of an image (150×100 pixels in our case) after pixel-to-pixel nonuniformity is removed subtracting two images. A factor of 2 must be included in the denominator when calculating the variance $\sigma_S^2(ADU)$, because when two identical images are subtracted or added the random noise or standard deviation of the resulting frame increases by $\sqrt{2}$. The variance $\sigma_s^2(ADU)$ of this differenced frame is given by:

$$\sigma_S^2(ADU) = \frac{\sum_{i=1}^{N_{pix}} [S_i(ADU) - S(ADU)]^2}{2N_{pix}} \tag{11}$$

- The abscissa is proportional to the exposure time or the average number of incident photons and photo-generated charge per pixel element. It is the mean in an area of an image (150×100 pixels in our case) that it is the result of two averaged images with the same exposure time.

The Fig. 29 shows an example of this curve. The data are taken at Fermilab with the back-illuminated CCD, s1-11, using a monochromatic light source at 800nm. The errors bar for the abscissa and ordinate values are calculated but are small to be seen in this scale. A linear fit to the data with the goodness of this fit is calculated to obtain the camera gain constant following the Eq.10. The inverse of the gain constant $(1/K)$ is $1.29 \pm 0.01\ ADU/e^-$. Note that the variance decreases highly when saturation occurs.

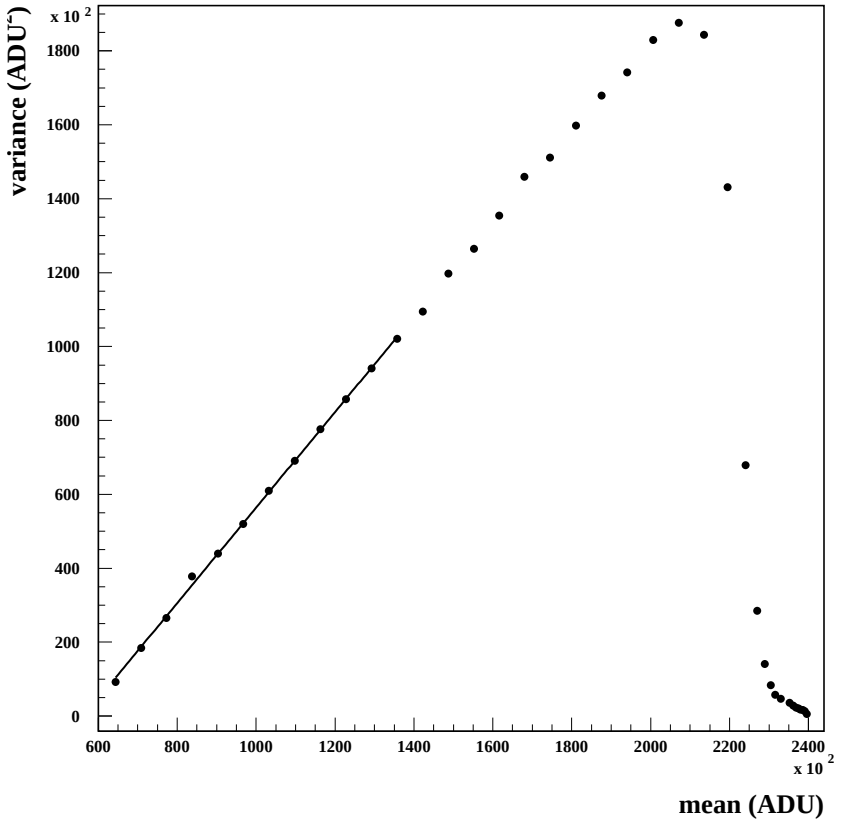

Figure 29: Photon Transfer Curve

An alternative method for obtaining this conversion factor between electrons and ADU is to use an image taken with an Fe^{55} x-ray source as explained in Sec. 4.3.2.

4.2.3 Readout noise

The readout noise floor is obtained by computing the spatial root mean square, rms, of the signal measured in the extended pixel region or serial overscan area of each output channel. This quantity is measured in each pair of images for every exposure time taken in the photon transfer curve. It is very difficult to disentangle the noise of the external electronic chain from the noise of the CCD on the chip amplifier, so it is preferred to consider the noise of the whole electronic chain.

After measuring the gain, the readout noise is converted from analog-to-digital units (ADU) to electrons.

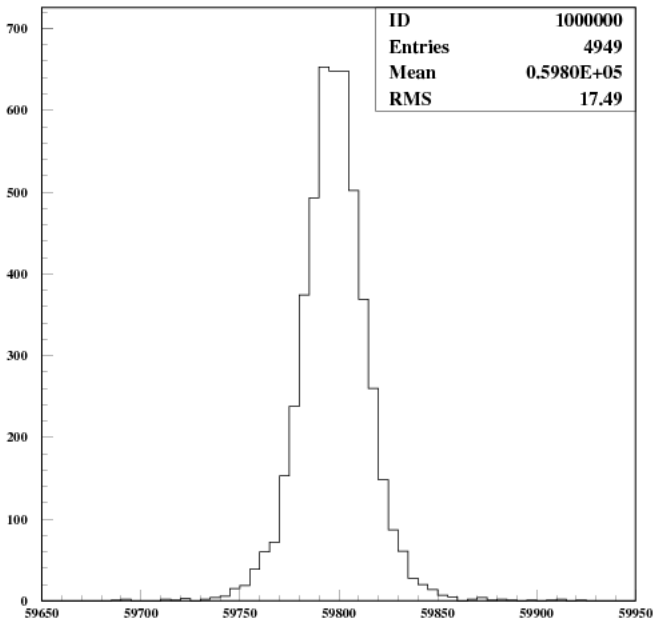

Figure 30: Histogram of the horizontal overscan area for s1-11 at 5.9μs/pixel.

The readout noise depends on the readout speed. The CCDs are tested at a nominal readout speed of 4μs/pixel. At present at FNAL 8 electrons readout noise are achieved at 3.7μs/pixel (a little better than the specifications on both accounts). The relevant specification requires $\sigma_R \leq 15$ e$^-$ for a readout speed of 250 kpixel/s (corresponding to 4 μs/pixel). These specifications are satisfied but considering that the environment at the telescope will be very different and probably noisier for the electronics with respect to the lab, the goal of $\sigma_R \leq 10$ e$^-$ at that speed is achieved too.

An example of a histogram of overscan signal to calculate the noise is shown in Fig. 30. The noise value is approximately 13 e$^-$ at 5.9 μs/pixel for a test made with

the s1-11 CCD.

4.2.4 Non linearity and full well

Nonlinearity is a measurement of the camera gain constant as a function of signal. Ideally there should be no dependence. In order to obtain the high precision that astronomy and cosmology require nowadays, we need high sensitivities out to low level signals and measurement uncertainties lower than 1%

The excellent linearity of these CCDs facilitates these requirements and allows image subtraction and flat-fielding to eliminate the backgrounds and instrumental artifacts. The mean of the signal level as a function of the exposure time is represented so the data obtained in the photon transfer curves are also used to check the linearity in the response of the device. An example of such study is shown in Fig. 31 with a linear fit to the data (green line).

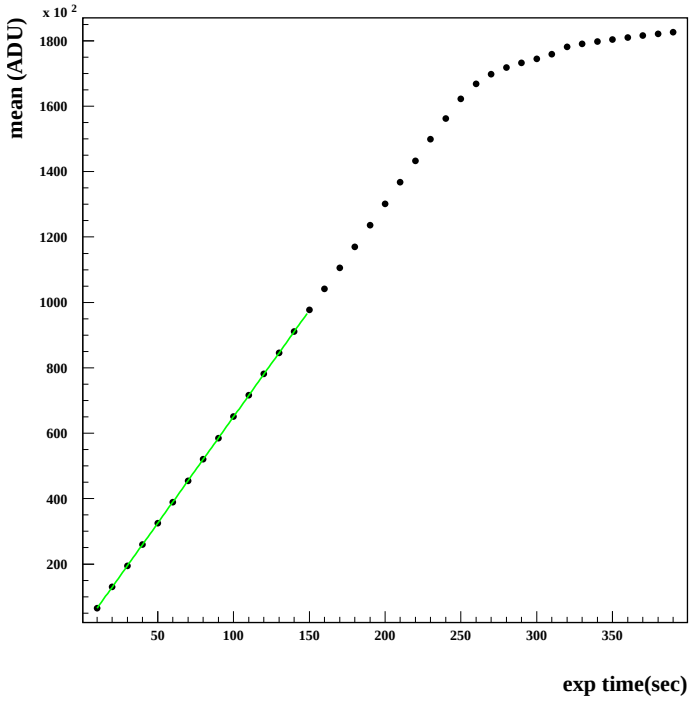

Figure 31: Mean as a function of exposure time

The plot in Fig. 32 shows the number of electrons calculated with the conversion factor or gain as a function of exposure time. In this case the data was collected with a gain setting selected to match the dynamic range of the readout electronics to approximately 130000 e^- value (green line). The errors in the mean are calculated but are

small to be represented in these plots ($\sim$ 100-1000 ADU).

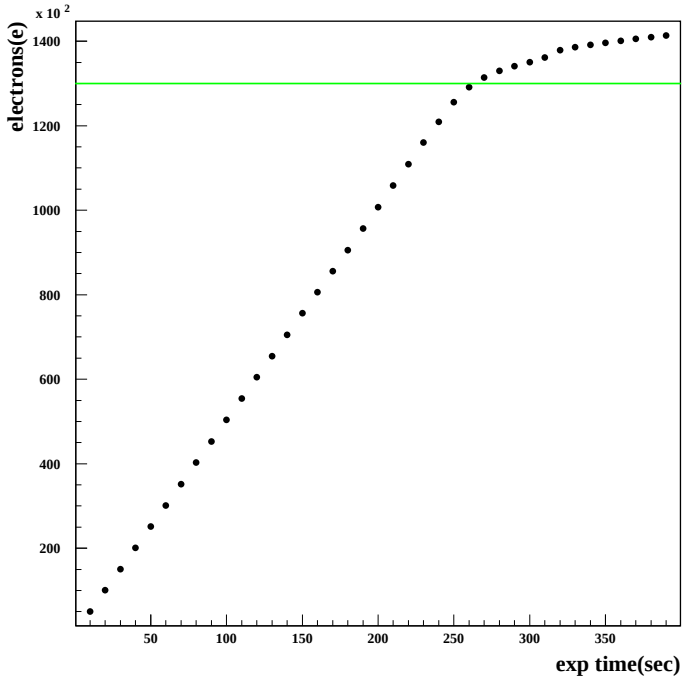

Figure 32: Charge Collected as a function of exposure time.

The full well or well capacity is the maximum charge level that the pixel can hold and transfer. It is measured as charge level at which the CCD starts to show a deviation from linearity of more than 1%. The relative residuals to the fit are shown in Fig.33. These (red lines) are between $\pm$ 1% for charge levels $\leq$130000 e^-.

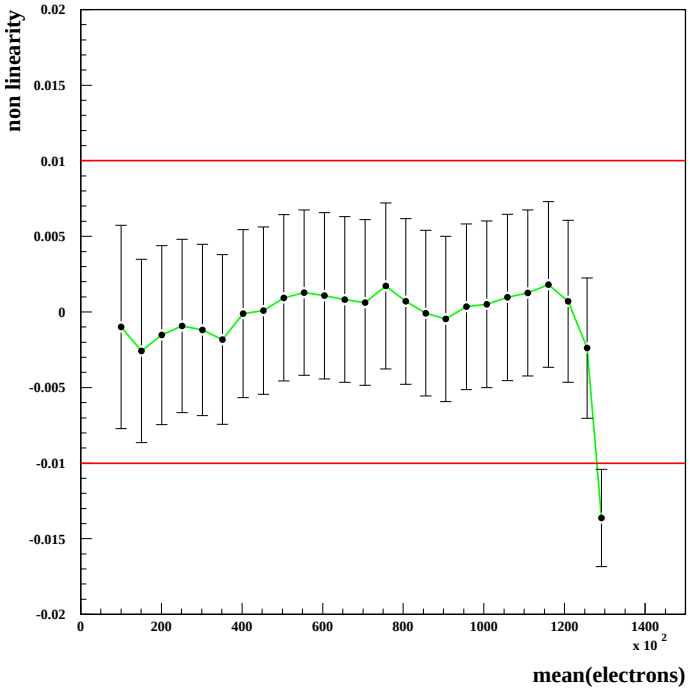

Figure 33: Relative residuals as a function of electrons

4.2.5 Photon Transfer Curve conclusions.

In each pair of images the pedestal and the readout noise is measured to test the correct operation of the camera. Both should be constant during all the operation time. The pedestal is the mean value of the signal in the overscan area. If the pedestal level shows a smooth variation of amplitude over the course of the test it will require overscan correction to the individual frames for the linearity curve.

This setup is being forced to use a long integration time (up to 390 s in our tests) for the higher signal level due to the slow shutter. This is a disadvantage on multiple levels. Not only is the test likely to take long time, the density of cosmic rays make it difficult to find a clear region. Nowadays at Fermilab the linearity test is done with an ascending and descending sequence pairs of frames of shorter integration times. This sequence is important to study and characterize easily the detector phenomena. The erase mechanism is used to eliminate some detector phenomena as the residual image produced by the saturation of the serial register after a saturated exposure. This makes the charge move from it to the active region of the detector and could affect the linearity curve. For that reason the ascending and descending sequence in the photon transfer curve is a good method to detect that phenomenon.

4.3 X-Ray Calibration

4.3.1 Introduction

A visible or near-infrared photon, interacting with silicon, generates a single e^-- h^+ pair. It would be instructive to observe the fate of such electron as it is drawn in the potential well and then transfered until its converted to an output voltage. However, current technology does not permit accurate measurements of such small charge. Instead, CCD characterization employes relatively large numbers of photons and the resulting data represents averages over a large number of pixels and are limited in their accuracy by the intensity, focus and stability of the source. To circumvent these requirements x-ray illumination to supplement visible light as calibration technique is used.

Soft x-ray photons (1 to 1000 Å) have much higher energy than do visible light photons. Absorbed by silicon, this additional energy generate multiple e-h pairs in the CCD. In contrast to the visible light case, the electrons are generated in a very small cloud diameter, essentially a near perfect point source. The 5.9 keV photons are absorbed $\sim$30 μm (63% of photons are absorbed) into the devices and generates a cloud of $\sim$1620 carriers (the energy required to generate an electron-hole pair is 3.65 eV/e^- for silicon) contained within a diameter of only $\sim 0.4\mu$m (full width at half maximum FWHM).

Ideally, the charge from a single x-ray photon would be confined to a single pixel (referred to a target pixel), and the surrounding pixels would contain no charge. In practice, the photon is sometimes absorbed belowthe CCDs depletion layer, in a field-free region. Charge generated there diffuses into neighboring pixels, an indicator of degraded charge collection efficiency. Also, imperfect charge transfer causes some of the charge from the target pixel to lag during successive transfers so that an x-ray event exhibits a tail of deferred charge. The size and shape of this tail is a sensitive indicator of charge transfer efficiency performance, see section 4.4.

X-RAY GENERATION

A Fe^{55} x-ray source is used for this calibration. This isotope is inherently unstable and decays into a Mn atom when a K-shell electron is quantum mechanically absorbed by the nucleus. An x-ray is generated when an electron drops from either the L- or M-shell to fill the empty K-shell. This action in turn produces either a K_α(5.9 KeV) or K_β (6.5KeV) x-ray with a ratio of approximately 7 to 1. This ratio is important to interpret the histograms of x-ray images because the K_α *is* the most prominent.

4.3.2 X Ray Images and Gain Calculation

Fig. 34 presents an image of a flat field of Fe^{55} x-ray events taken with the 2k$\times$4k pixels pf-24-25 CCD. Each dot represents a measured electron and is positioned within the pixel in which it was detected. A source of 100 μC Fe^{55} is used because it is physically small and can be placed a few inches from the CCD to provide uniform illumination. This is possible because the dewar used has an knob accessible from the front face that when turned, presents the x-ray source to the front of the CCD.

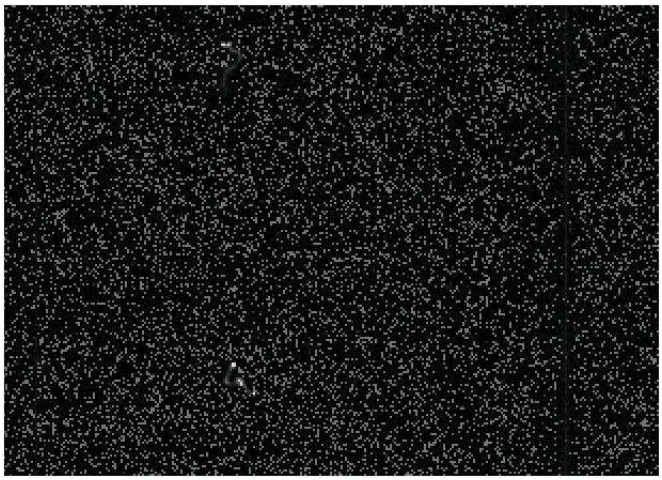

Figure 34: Flat field image of Fe^{55} x-ray events.

An alternative method for obtaining the gain of the conversion factor between electrons and ADU is the Fe^{55} x-ray spectrum. This technique and the technique to measure the CTE that will be explained in section 4.4 is based on the assumption that the energy deposited by an x-ray hit is restricted to one pixel. Because the DECam detectors are 250μm thick and back illuminated the charge diffusion makes the assumption of single pixel hits non valid. The electron holes will travel several hundreds μm through silicon before they get collected in the gate structure. Depending on the strength of the depletion field and the device thickness the charge packet can spread out and end up in more than four pixels. However, these CCDs can be packaged as front illuminated detectors and exposed to x-rays from the front to study CCDs with this method. In this case, the x-ray generate e^-- h^+ pairs close to the gate structure. Only if an x-ray hits the edge of the corner of one pixel, the resulting charge might spread over several pixels. The charge will usually be contained in one pixel. In most cases it won't spread to more than four pixels.

The Fig. 35 shows the x-ray spectrum measured for the detector with an exposure of 40 s. The overscan has been subtracted. The plot shows two main peaks, the leftmost one corresponding to the pedestal, only the dark counts collected in the pixel, and the rightmost one corresponds to the 1620 e^- deposited in single pixel hits by x-ray of 5.9 keV. A less significant peak corresponding to 6.5 keV is also seen.

Therefore the gain is directly derived from the measurement of the mean signal of these two peaks in the histogram of the distribution of hits as Fig. 36 shows.

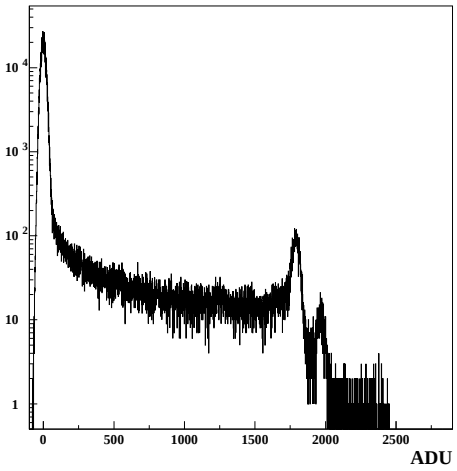

Figure 35: X -ray spectrum with the overscan subtracted. The K_α and K_β are shown.

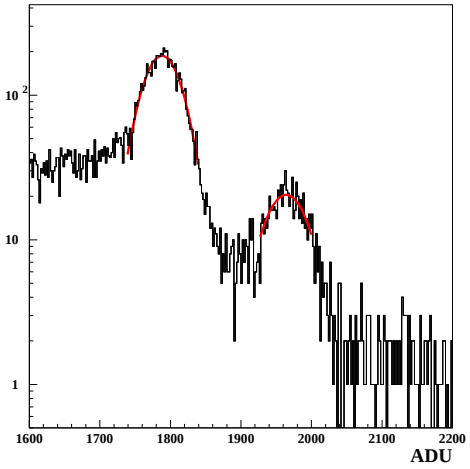

Figure 36: Calculation of K_α and K_β peaks.

The means and root mean square obtained when a fit to a Gaussian of the peaks is made are:

S_α = 1790 ADU ; σ_{S_α} = 30 ADU

S_β = 1960 ADU ; σ_{S_β} = 30 ADU

Knowing that the generated electrons by K_α and K_β lines are 1620 e^- and 1778 e^-

respectively, the gain for both calculations is 1.10±0.02 ADU/e^-. The result obtained with the photon transfer curve for this CCD is K = 1.12±0.01. The measurements made with this two methods agree at the 1 sigma level. The x ray method is somewhat more inaccurate due to charge diffusion and the uncertainties in the calculation of the peaks. However, it has the advantage of taking less time to obtain the gain value.

The error of the gain is very important in the determination of the quantum efficiency, charge diffusion and traps. The QE parameter is the ratio of incident photons to generated electron-hole pairs. Thus, uncertainties of the gain or the calibration are very significant sources of systematic errors in the measurements of the QE.

4.4 Charge Transfer Efficiency

The charge transfer efficiency CTE denotes how much of the charge in one pixel actually gets transferred into the next pixel in a three phase clocking time. The importance of this parameter is easily understood if we take as an example a CCD with a CTE of only 99%. In a 100×100 pixels large CCD the charge of one pixel might get shifted as often as 100 times in the vertical direction before it reaches the serial register. Now, if during each clocking cycle one percent of the charge is lost, only 0.99^{100} = 0.37 = 37 % of the original charge reaches the serial register.

The biggest DES devices are about 2024×4096 pixels. With the readout system the whorst is the case when the charge has to be shifted 4096 times. Obviously such a device would be unusable with 99% CTE. Buried channel CCDs typically have a CTE of 0.99999% or higher as it is obtained in the test.

Several methods exist to measure the CTE. In this work it is determined by both the use of a Fe^{55} source and by the extended-pixel-edge-response (EPER Method). These are explained with examples in Sec. 4.4.1 and Sec. 4.4.2 respectively.

4.4.1 X-Ray Transfer Method

X-ray transfer is the standard method in measuring absolute CTE performance. If the amount of electrons which result from a x-ray photon absorption is known, one can estimate the CTE by simply comparing this number with the number of measured electrons at the readout amplifier. The most prominent feature in the x-ray energy spectrum is a 5.9 keV line. In most x-ray hits all of the energy is deposited into one pixel. The ratio of measured charge with respect to expected as a function of pixel position in the detector charge provides the charge transfer inefficiency (CTI). As explained before, because of diffusion in 250 μm-thick back illuminated CCD the charge is spread out. However, the CTI is measured in packages built with the front side exposed (2024×4096 pixels CCDs of 650μm thickness).

For the transfer plot all columns or rows are stacked together in a single plot. The vertical axis is expressed in ADU units. For the horizontal CTE the signal per pixel is plotted vs. the column number or number of times that the charge has to be transferred for one pixel to the other after the video signal is digitalized. For the vertical CTE the abscissa is the row number or number of times to be transferred before being read out at the sense node.

Fig. 37 shows the transfer plot to measure the horizontal CTE (serial CTE) for the pf-24-25 CCD. The strong signal level seen at around 1700 ADU represents the single-event pixel line (K_α events). Signal below this dark band are x-ray events where the charge was split into multiple pixels. The circles represent the mean of the position of the K_α peak, mean in ADU with the pedestal subtracted, in intervals of 100 columns. The slope of the K_α bands gives the horizontal measure of CTE.

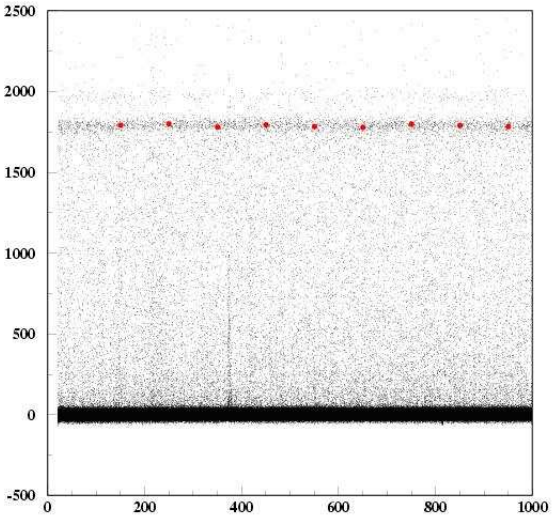

Figure 37: Horizontal x-ray transfer. ADUs in the Y-axis as a function of column number.

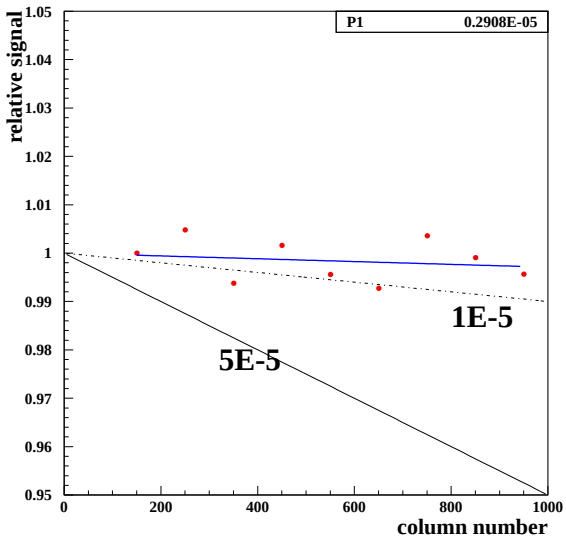

Figure 38: Horizontal CTI measurement .

Fig. 38 shows the fraction of charge measured for 5.9 keV ray peak as a function of column number. A fit with the function 1-P1*x is made (blue line). The slope (P1) is the horizontal CTI and x is the column number. Two example lines are shown for CTI equal to 1×10^{-5} and 5×10^{-5}. The relative values of the charge don't show clearly a decrease with the column number as it will be expected and its errors are too high ($\pm$0.025). The data are consistent with CTI $\sim$ 3x10^{-6} although the error in the slope (5×10^{-4}) is great enough to say only that the CTI could be lower than 5×10^{-4}.

The same exercise for the vertical CTI of pf-24-24 CCD gives approximately a value of 6×10^{-6} and also a great error in the slope (1×10^{-4}). The results are shown in Fig. 39 and Fig. 40.

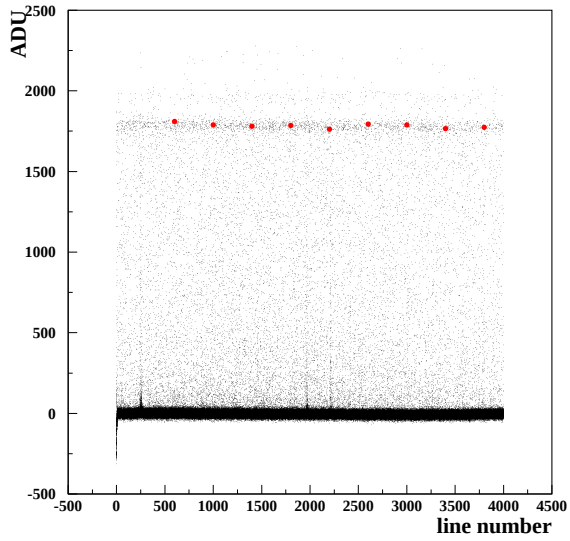

Figure 39: Vertical x-ray transfer. ADUs in the Y-axis as a function of row number.

The conclusion is that the errors in the slope using the x-ray method are too high and therefore one can only say that the CTI measured at the standard operating voltage is consistent with CTI lower than 10^{-4}. The main error sources are in the calculation of the values that distinguish between the charge deposited by the x ray hits and the pedestal value. They have a high standar deviation. The diffusion effect that makes the charge packet spread out could also affect to this measurements. In addition, when CTE $>$ 0.99998 and N$_P$ $>$ 1024 as in our case this method to obtain the transfer efficiency becomes imprecise (i.e. the tilt in the line is difficult to measure) [4].

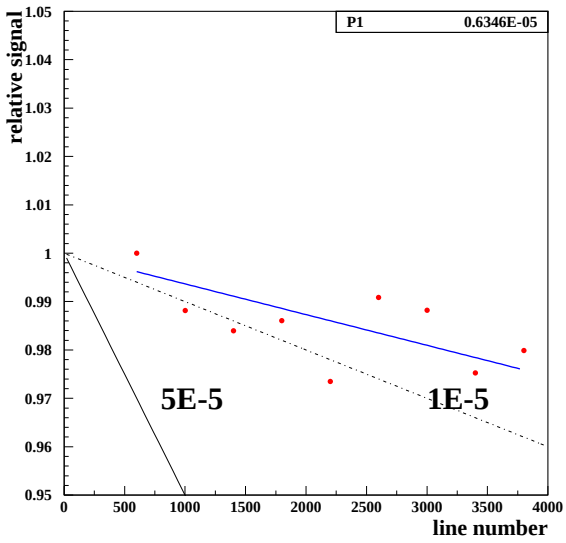

Figure 40: Vertical CTI measurement.

4.4.2 The Extended Pixel Edge Response (EPER) Method.

The method used to calculate the CTI for the back-illuminated CCD is the Extended Pixel Edge Response although the examples shown here are from a front illuminated CCD to compare with the x-ray transfer results. The EPER begins with a flat field exposure of 10 s with the subsequent readout of a number of trailing pixels which is more than the physical number of pixels in the CCD in order to obtain overscan areas in both directions. CTE is estimated by measuring the amount of deferred charge found in the extended pixel areas.

In the EPER plot several rows or columns are averaged together to reduced the noise and improve the S/N ratio in the overscan area. Then the pedestal or overscan is subtracted and these data are normalized to the mean value in the physical pixel area. The ordinate axis value versus the column or row number is given by

$$\frac{S_i - S_{overscan}}{S}$$

where S_i is the averaged signal en each column or row, $S_{overscan}$ the averaged signal of the overscan region and S is the mean signal of the physical pixel area with the overscan subtracted. If

$$\eta = \frac{S_D - S_{overscan}}{S}$$

where S_D is the averaged signal at the first pixel in the overscan, then CTE from an EPER plot is defined as

$$CTE = 1 - CTI = 1 - \eta/N_P$$

where N_P is 1024 for the horizontal and 4096 for vertical CTI in 2k$\times$4k pixels CCD, read with two amplifiers. The charge for the last physical pixel has to be shifted 1024 and 4096 respectively before it is readout.

4.4.3 Clock Rail Scan. CTE Results with the EPER Method.

The CTI, in practice, depends on the levels of various CCD clocks. For this reason, a single set of clock voltages for which all the CCDs pass the CTI technical requirement (TD. 14 in Appendix A) for both horizontal and vertical clocks is found. These are the operating voltages used.

In the Clock Rail Scan each of the four clock rails (horizontal upper and lower rail, vertical upper and lower rail) used for the charge transfer between pixels is varied between 0.5 V and 10 V in steps of 0.5 V. A 10 s exposure is taken for each voltage level. This scan is performed to verify the technical requirement on charge transfer efficiency. The CTI for a typical device is $10^{\cdot 7}$ at the operational voltages. Since a set of clock levels is found that meets the requirements for every CCD, this step is not strictly necessary. However, it is useful to verify the CTE and the noise dependence on the clock level for each CCD. The test also allows to understand the possible dependence of any defect on the clock levels.

EPER plots examples are shown in Fig. 41 and Fig. 42. They represent the transition between the readout of the physical pixels and the overscan as a function of the horizontal barrier H+ phase and the collecting H- phase respectively for one amplifier. In both figures the error bars are represented. For a perfect transfer efficiency the transition between the exposed area (columns lower than 181) and the overscan should be perfectly sharp, going from 1 to 0 in this scale. For H- the transition is always very sharp corresponding to a good CTE.

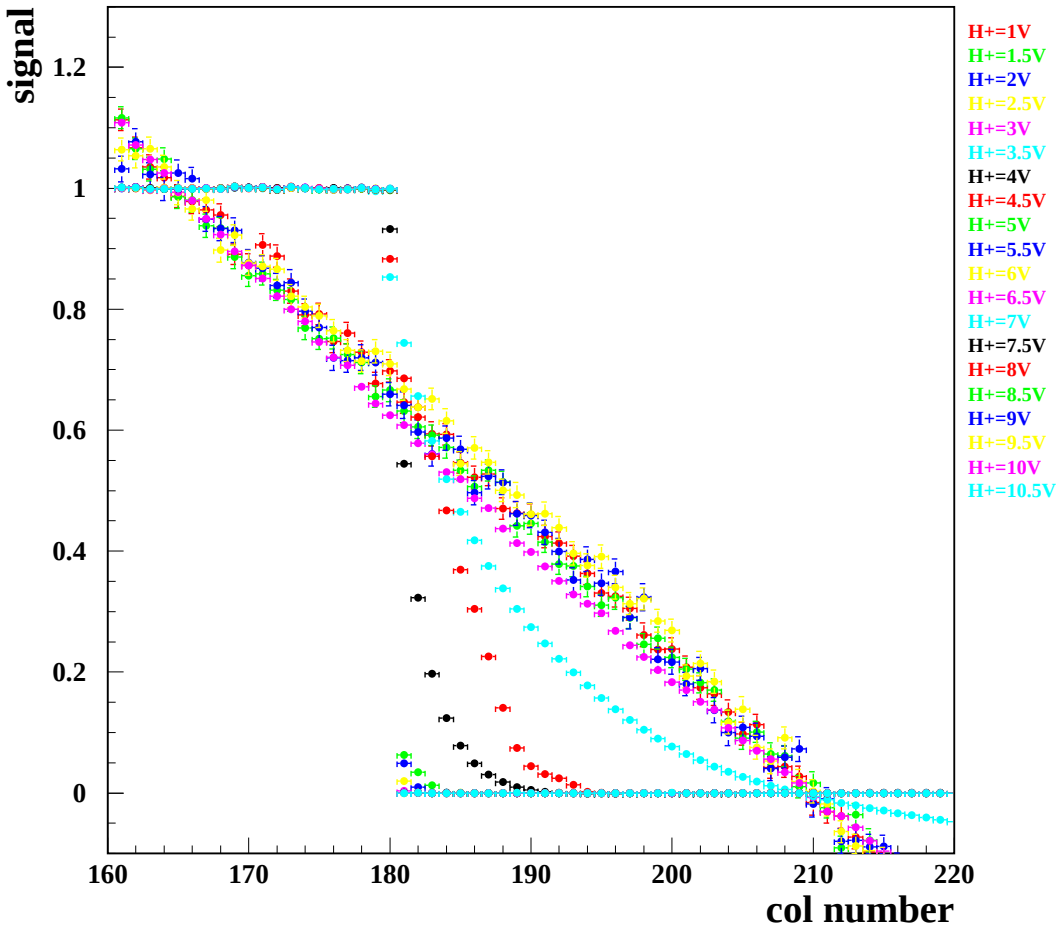

Figure 41: EPER plot for H+

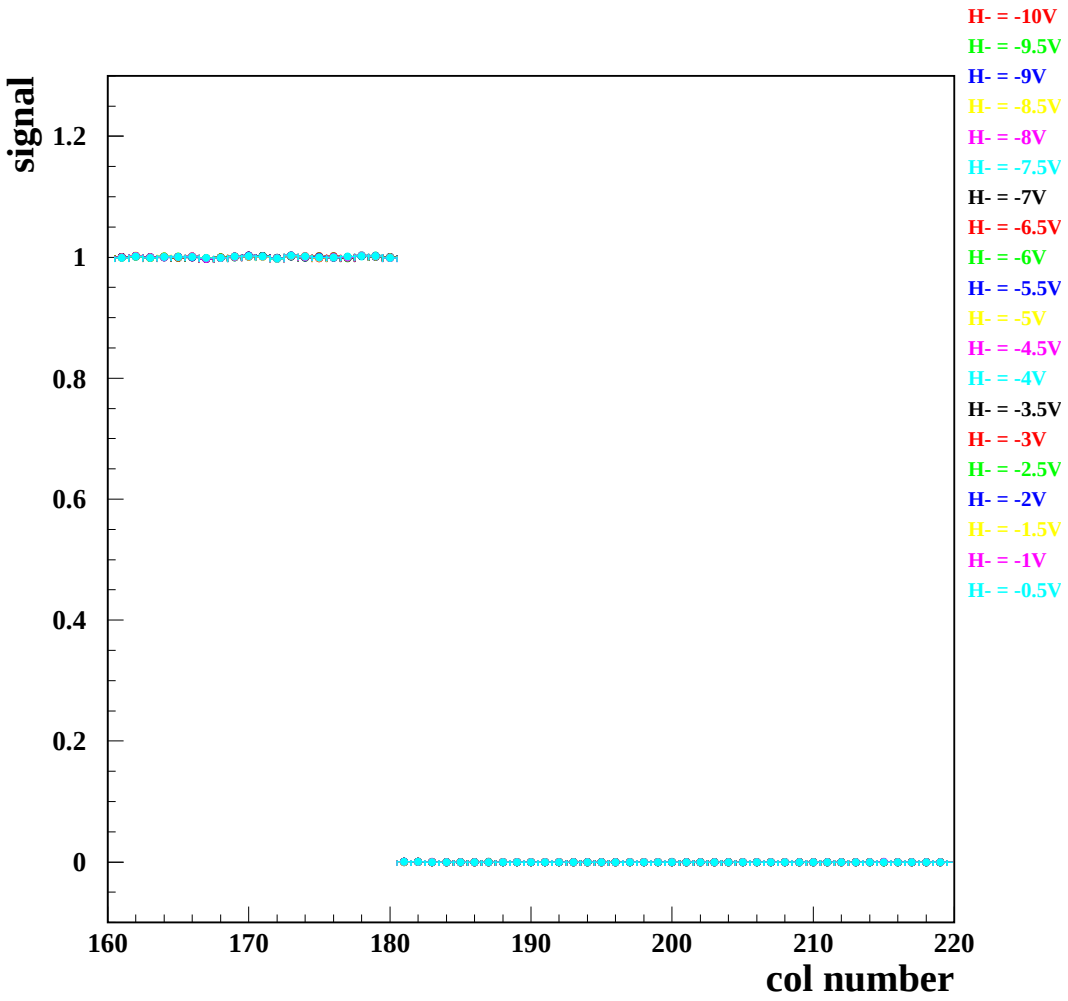

Figure 42: EPER plot for H-

The CTI is calculated with the values obtained in the EPER plot. The top plots of Fig. 43 and Fig. 44 show the serial CTI as a function of the voltages. The requirement value is achieved at barriers voltages (V+) higher than 6 V and for all values of the collecting voltages (H-), therefore in these CCDs the transfer efficiency is controlled by the positive barrier phase. The collecting phase controls the optimum full well capacity but this last will not be studied here in detail.

The results for the operating voltages show that the CTI is approximately equal in both calculations, CTI = $1.9\text{x}10^{-7} \pm 0.6\text{x}10^{-7}$ for H+ = 8.5 V and CTI = $1.2\text{x}10^{-7} \pm 0.5\text{x}10^{-7}$ for H- = -3.5 V.

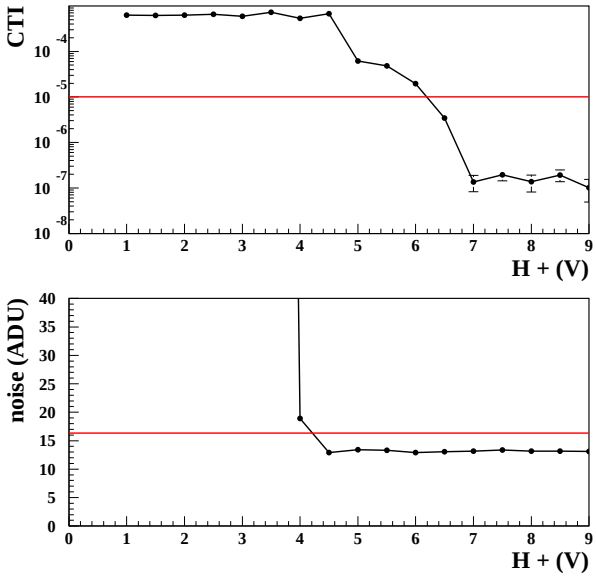

Figure 43: CTI and noise for H+ values

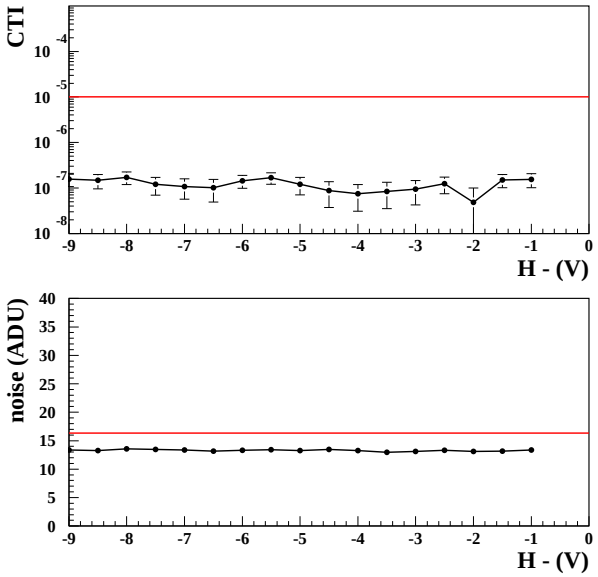

Figure 44: CTI and noise for H- values

At the bottom of the same figures the noise measured as a function of the horizontal voltage H+ and H- is plotted. In the former the noise remains constant with H+ until inversion is reached at 4V. At that point spurious charge is likely generated, resulting in a noise increase. Therefore, the horizontal register is normally biased out of inversion. However, in the latter the noise remains constant for the collecting phases. The red line is the value imposed by the noise requirement. Therefore, the operation of our CCDs with the values chosen for the H+ and H- voltages at the pixel rate used satisfy this requirement.

For the calculation of the vertical CTI the same exercise is done. See Fig. 45 and 46.

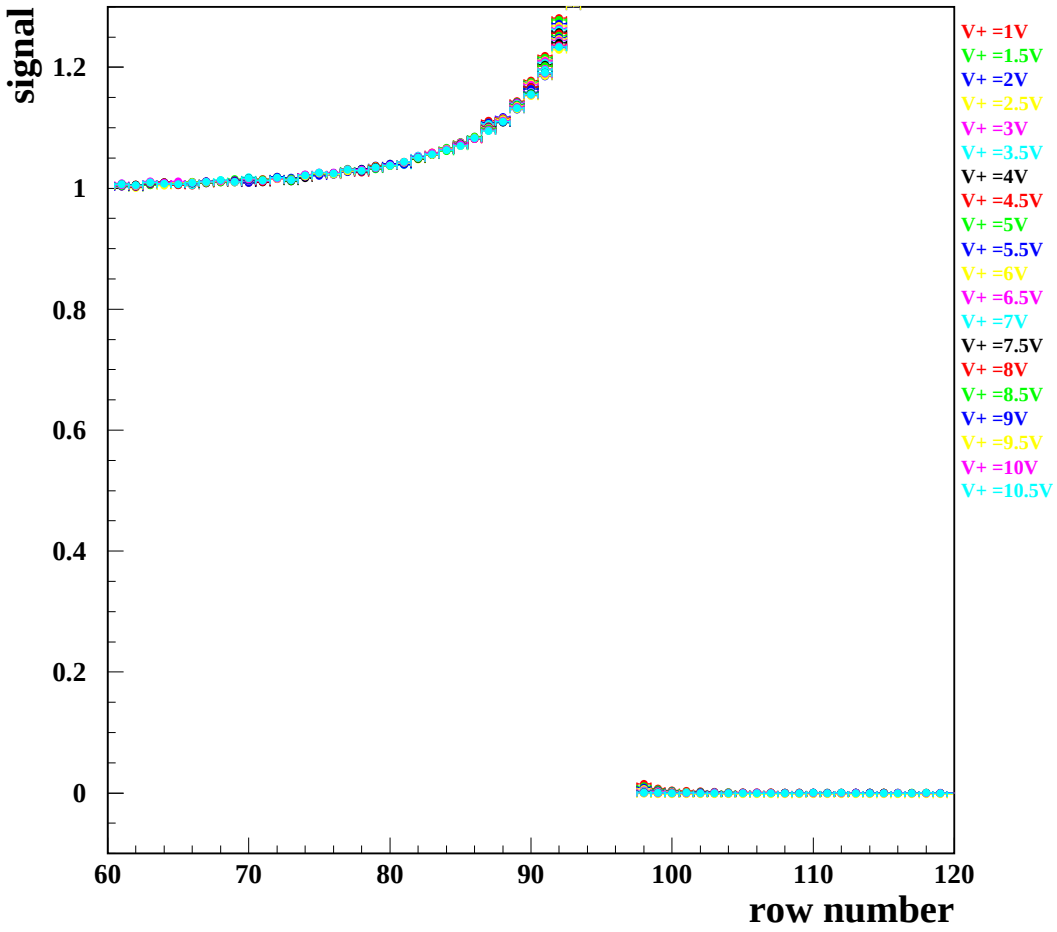

Figure 45: EPER plot for V+

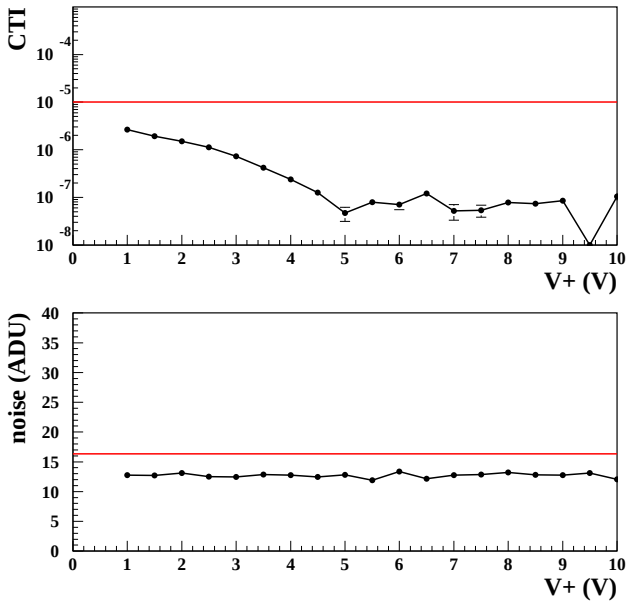

Figure 46: CTI and noise for V+ values

The CTI found at operating values (V+ = 5.5V) is approximately $8\times10^{-8} \pm 2\times10^{-8}$. Because of the increment of the effective size of the pixels of the last rows the signal increases in the last rows of the physical pixel area. This effects is called glowing edge and adds imprecision in the vertical inefficiency measurements.

4.4.4 CTE conclusions

The EPER technique must be used with caution because it is a relative CTE test tool. It does not give an absolute measurement for CTE as the x-ray test does. However, because of the high diffusion in back illuminated CCDs, the high values of N_p and CTE, the x-ray technique is imprecise too, therefore EPER is a valid technique for our case and will be the testing method to measure the CTE in the production phase.

The EPER also overestimates CTE performance, sometimes significantly. A CCD with a CTE problem will not show deferred charge as measured by EPER [4]. An example would be a CCD damaged with neutrons that generates low level traps and CTE degradation. The deferred charge tail is sometimes eliminated suggesting that CTE has been enhanced by clocking faster. But the amplitude of the dark spikes (signal test) induced by neutrons remain constant independent of clock rate. This indicate that CTE is not improving, or the dark spike amplitude would increase. See ref. [4] for details.

Despite the error sources in the EPER and x-ray methods that could explain the

differences between the results obtained with both techniques for a front illuminated, it is not possible to draw conclusions from the comparision of these measurements due to the high errors found in the measurement of the charge deposited and its transference with the x ray method. More studies (as diffusion in front and back illuminated devices), new data and the reduction of the pedestal noise to distinguish the charge deposited by the x ray should be performed. However, even with these improvement plans this x ray technique could be still imprecise due to the high Np and CTE of these CCDs.

The CTE is a parameter that also changes with transfer rate and with the illumination level. The effect of charge traps in the CTE is another test that should be studied in the performance of the testing station.

5 Conclusions

The main goal of this research work is to describe and understand a system to cool down CCDs and to gain experience about some techniques to characterize the LBLN CCDs. Some examples of these tests are explained with data that I took at Fermilab and then analyzed. These CCDs will be employed in the Dark Energy Survey project.

In Barcelona (IEEC, IFAE) all the tools and instrumentation of chapter 3 was implemented. That includes the mechanical construction of the dewar and the development and control of the vacuum and the cooling system. Currently the setup is in an initial phase to reduce the noise levels and improve the measurements. All the CCD testing methods of the chapter 4 have also been tested in Barcelona with the S-Link optical fiber connections. But due to noise levels and other error sources the examples are not shown. The important thing is that the system built and developed in Barcelona is able to do the tests described although further work has to be done. To characterize a CCD more techniques have to be developed to satisfy the rest of the requirements and some errors sources eliminated. For this purpose the optical setup and electronics has to be developed and controlled.

The noise reduction is the first task that should be done although it is no easy and requires the study of its variation with the readout speed. As it is explained in Sec. 4.2.5 an erase mechanism to eliminate the residual image produced by saturation of the serial register is needed. This mechanism must be done after every test exposure because could be an important error source in the linearity calculation, for instance.

Detailed studies of the cosmetic defects in the devices should be performed to complete the Testing Stage 1 described in Sec. 2.3. These requirements are checked taking long dark exposures, flat exposures at different light levels and by doing charge pumping to detect traps. This last defect (traps) is an error source for the calculation of the CTE value, for instance. For this reason, their positions and their mean values should be measured.

Further analysis should be done to characterize a CCD and complete the Testing Stage 2. For this purpose the measurement of the quantum efficiency and the diffusion values will be performed as well as the temperature studies of the dark current and quantum efficiency.

The measurement of the quantum efficiency takes a long time because first, the optical setup must be well calibrated and provides flat field images with an uniform and parallel beam light. The diffusion value will be measured as a function of the substrate voltage. Different methods could be used, for instance, using a diffraction pattern or an x ray source. The election of the method and its development could be an interesting object of investigation.

It is very important to control automatically the instrumentation if the temperature studies mentioned before and the rest of the testing stage 2 methods will be carried out. Otherwise, many hours will be spent taking data.

In conclusion, all the parameters measured in this work are well understood and satisfy the technical requirements at FNAL CCD Testing lab. These are the camera gain constant (no requirement), the linearity, the full well and the charge transfer efficiency. Due to the high diffusion the use of an x ray source for the gain and CTE calculation is not valid for the back illuminated CCDs that will populate the camera. However,

it could be used as a technique to measure the diffusion in this type of CCDs. In this work the CTE and gain are also measured with an x ray source because the first tests in the initial and training phase were done with front illuminated CCDs. An example to compare their results with other techniques that use a light beam is explained. The results given tell us that, although the calculation of the CTE is very inaccurate, the gain result agree in both methods.

A complete report with the analysis results is done after the Testing Stage 1 data are taken. It is important to mention that I have been involved in these tasks.

6 Acknowledgements

The work described in this document was done from June 2005 to October 2007 at Instituto de Ciencias del Espacio (ICE-CSIC/IEEC), Instituto de Fisica de Altas Energias (IFAE) in Bellaterra, Barcelona and at Fermi National Laboratory (FNAL) in Chicago, USA. I want to thank all people who support me there.

Especially:
Juan Estrada from FNAL who taught me all the characterization techniques.
All the people from the Fermilab CCD Testing Group, especially Tom Diehl, Herman Cease and Bob Angstad who explained me the cryogenic and vacuum system as well as the Tcl/Tk software to make the Monsoon system works and start to test the CCDs in Barcelona.
Donna Kubik who helps me with the CCD testing reports.
Vittoria Finazzi from ICE-CSIC/IEEC that help us with the dewar construction and vacuum system in Barcelona.
Laia Cardiel from IFAE for the work with the electronics, the dewar construction and vacuum and cryogenic system in Barcelona.
Francisco Javier Castander Serentill from ICE-CSIC/IEEC who was my director.
Marino Maiorino who work with the optical instrumentation and help me to write this work and to carry the heavy LN_2 dewar to fill and cool the cryostat and people from IFAE and ICE who supervise my work.
Josep Guerrero from ICE for the computing and Linux support.
All the partners that work in the ICE and all the others I didn't mention in person.

This work was supported in part by Ministerio de Educación y Ciencia (MEC), under contract AYA2005 and AYA2006-06341, and by Generalitat de Cataluña, under contract 2005SGR00728.

7 Appendix A

The following table shows the technical specification for the DES CCDs.

Measurement	DeCam Requirement	Technical Specification
QE(g,r,i,z)	60%, 75%, 60%, 65%	TD.7
QE Instability	< 0.3% in 12-18 hrs	TD.8, TD.9
QE Uniformity in focal plane	< 5% in 12-18 hrs	TD.10, TD.11
Full well capacity	> 130.000 e-	TD.2
Dark current	< ~25 e-/hr/pixel	TD.5
Persistence	Erase mechanism	TD.3
Read noise	< 15 e- @ 250kpix/s	TD.4, TD.12
Charge Transfer Inefficiency	$< 10^{-5}$	TD.6
Charge diffusion	1D σ< 7.5 μm	TD.13
Cosmetic Requirements	# Bad pixels <0.5%	TD.16
Non Linearity	< 1%	TD.1
Package Flatness	See text.	TD.14, TD.15

Table 3: Technical specifications for DES CCDs.

8 Part List

INSTRUMENT	MODEL NUMBER
Turbomolecular pump	TMU 071 P Pfeiffer
Diaphragm pump	MVP 015-4 Pfeiffer
Vacuum gauge	PKR251 Pfeiffer Compact Full Range
Flow meter	RMA-13-SSV
Relief Valve	Circle Seal Controls 200 Series 1”
Temperature Controller	Lakeshore Temperature Controller 332S
Temperature Sensor	Lakeshore DT-471-ET Silicon Diode
Heater	Lakeshore HTR-25-100 Heater Cartridge
Sensor wire	non-magnetic wire 32 AWG

Table 4: Vacuum and cryogenic instrumentation.

INSTRUMENT	MODEL NUMBER
Lamp	Quartz Tungsten Halogen lamp
Power Supplies for Lamp	Newport 68938
Filter Wheel	Newport Oriel 74040
Condensing Lens Assembly	Newport 60076
Electronic Shutter	Newport 68938
Integrating Sphere	Newport Oriel 70451
Baffle	Fermilab

Table 5: Optical Instrumentation at Fermilab.

The Tab.5 list the instrumentation at Fermilab because the test data used in this work were taken from there.

List of Figures

List of Tables

References

[1] E. Holland, et al, ”Fully-Depleted, Back-Illuminated Charge-Coupled Devices Fabricated on High-Resistivity Silicon”, IEEE Trans. Elec. Dev, vol. 50, no.1, pag. 225-338, 2003

[2] Douglas L. Tucker et al, ”The Photometric Calibration of the Dark Energy Survey”. Dark Energy Survey Document.

[3] S.B. Howell, ”Handbook of CCD Astronomy”, Cambridge University Press 2006

[4] James R. Janesick, ”Scientific Charges Couples Devices”, SPIE Press 2001

[5] J. Estrada, et al, ”Comparision of DECam engineering CCDs with the DES technical requirements”, Dark Energy Document 479 v-5 for Technical Review, April 2007

[6] P. Borgeaud et al, ”The 40 CCDs of the MegaCam Wide-Field Camera: Procurement, Testing and First Laboratory Results” , Proc. SPIE Vol. 4008, Pag. 356, 2000

[7] H. Oluseyi et al, ”Characterization and deployement of large format, fully depleted, back illuminated, p-channel CCDs for precision astronomy”, in the proceedings of Sensor, Systems and Next Generation Satellites”, edited by R. Meynart, S.P. Neeck, H. Shimoda, SPIE 5570, 514-524, September 2004

[8] J. Estrada et al, ”CCD testing and characterization for Dark Energy Survey”, Proc. SPIE Vol. 6269, June 2006

[9] G. Derylo, H. Thomas Diehl and J. Estrada, ”0.25 mm thick CCD packaging for the Dark Energy Survey Camera Array”, Proc. SPIE Vol. 6276, June 2006

[10] ”LBNL CCD web page”: http://www-ccd.lbl.gov/

[11] P. Amico, T. Bohm, C. Cavadore, ”The ESO CCD testbench”: http://www.eso.org/projects/odt/CCDtestbench/Testbench.html

[12] ”Dark Energy Survey Collaboration Web Page”: https://www.darkenergysurvey.org

[13] J. Annis, ”The Dark Energy Survey, Technical Specifications Document”, DES Document.

[14] ”DES Document Database”: http://des-docdb.fnal.gov/

[15] ”Lakeshore web page”: https://www.lakeshore.com

[16] T. Abbot, J. Abbot, J. Estrada, B. Flaugher and W. Merrit, ”The Dark Energy Camera (DECam) Project, Conceptual Design Report”, Version 1.9.3 April, 2007, DES Document 78-v32

[17] D. Galadí-Enriquez and Ignasi Ribas Canudas, ”Manual Práctico de Astronomía con CCD”, Ed. Omega 1998